minerals

MDPI

Article

Geochemical Evidence for Genesis of Nb–Ta–Be Rare Metal Mineralization in Highly Fractionated Leucogranites at the Lalong Dome, Tethyan Himalaya, China

Jiangang Fu [1,*], Guangming Li [1], Genhou Wang [2], Weikang Guo [1], Suiliang Dong [1], Yingxu Li [1], Hai Zhang [1], Wei Liang [1] and Yanjie Jiao [1]

[1] Chengdu Center, China Geological Survey (Geosciences Innovation Center of Southwest China), Chengdu 611230, China; 13982257109@163.com (G.L.); gwk_987@126.com (W.G.); dongsuiliang@163.com (S.D.); pzhliyingxu@126.com (Y.L.); zhanghai--2001@163.com (H.Z.); lwcugb@126.com (W.L.); ajiaocd@gmail.com (Y.J.)

[2] School of Earth Sciences and Resources, China University of Geosciences (Beijing), Beijing 100083, China; wgh@cugb.edu.cn

* Correspondence: fujiangangcd@163.com

Abstract: Leucogranites in the Lalong Dome are composed of two-mica granite, muscovite granite, albite granite, and pegmatite from core to rim. Albite granite-type Be–Nb–Ta rare metal ore bodies are hosted by albite granite and pegmatite. Based on field and petrographic observations and whole-rock geochemical data, highly differentiated leucogranites have been identified in the Lalong Dome. Two-mica granites, albite granites, and pegmatites yielded monazite ages of 23.6 Ma, 21.9 Ma, and 20.6 Ma, respectively. The timing of rare metal mineralization is 20.9 Ma using U–Pb columbite dating. Leucogranites have the following characteristics: high SiO_2 content (>73 wt.%); peraluminosity with high Al_2O_3 content (13.6–15.2 wt.%) and A/CNK (mostly > 1.1); low TiO_2, CaO, and MgO content; enrichment of Rb, Th, and U; depletion of Ba, Nb, Zr, Sr, and Ti; strong negative Eu anomalies; low εNd(t) values ranging from −12.7 to −9.77. These features show that the leucogranites are crust-derived high-potassium calc-alkaline and peraluminous S-type granites derived from muscovite dehydration melting under the water-absent condition, which possibly resulted from structural decompression responding to the activity of the South Tibetan detachment system (STDS). Geochemical data imply a continuous magma fractional crystallization process from two-mica granites through muscovite granites to albite granites and pegmatites. The differentiation index (Di) gradually strengthens from two-mica granite, muscovite granite, and albite granite to pegmatite, in which albite granite and pegmatite are highest (Di = 94). The Nb/Ta and Zr/Hf ratios of albite granite and pegmatite were less than 5 and 18, respectively, which suggests that albite granite and pegmatite belong to rare metal granites and have excellent potential for rare metal mineralization.

Keywords: monazite and columbite ages; whole-rock geochemistry; highly fractionated leucogranites; Nb–Ta–Be rare metals; Lalong Dome; Tethyan Himalaya

Citation: Fu, J.; Li, G.; Wang, G.; Guo, W.; Dong, S.; Li, Y.; Zhang, H.; Liang, W.; Jiao, Y. Geochemical Evidence for Genesis of Nb–Ta–Be Rare Metal Mineralization in Highly Fractionated Leucogranites at the Lalong Dome, Tethyan Himalaya, China. *Minerals* **2023**, *13*, 1456. https://doi.org/10.3390/min13111456

Academic Editor: Jean-Michel Lafon

Received: 20 September 2023
Revised: 8 November 2023
Accepted: 13 November 2023
Published: 19 November 2023

1. Introduction

Rare metal granites and pegmatites have diverse chemical signatures and are important sources of strategic metals, such as Li, Be, Nb, Ta, W, and Sn [1–6]. Granitic pegmatites are always grouped into two different families: LCT (from Li–Cs–Ta) and NYF (from Nb–Y–F). LCT pegmatites are overall more common than NYF [7]. These rocks often represent the transition between the magmatic and the hydrothermal stages, and this transition is very important for rare metal mineralization [1]. Understanding mineralization processes is essential for the exploration and optimal exploitation of rare metal granites and pegmatites for metals such as Li, Be, Nb, Ta, Rb, and Cs [6]. Two leucogranite belts have been recognized in the Himalayan orogenic belt: the Higher Himalayan and Tethyan

Himalayan leucogranite belts [8,9]. Leucogranites in the Tethyan Himalaya are always exposed in the domes in the North Himalayan Gneiss Domes (NHGDs). There is now general agreement that the Tethyan Himalayan leucogranites are often highly evolved granites [10–14]. Although highly evolved granites are mostly rare metal granites, there are currently very few typical rare metal deposits in the Tethyan Himalayan belt, aside from the Cuonadong skarn-type Be–W–Sn rare metal deposit in the Cuonadong Dome [15–17]. As for the relationship between leucogranites and rare metal mineralization in the Himalayan belt, previous research mainly focused on mineralogy for Be-, Nb-, Ta-, and Li-bearing rare metal minerals and geochemistry for whole rocks [8,18–20], which are characterized by poor representation.

The Lalong Dome, one of the typical domes from the NHGD in the Tethyan Himalayan belt, is located at the eastern part of the Tethyan Himalayan belt, between the well-studied Kangmar and Cuonadong Domes. Leucogranites, including two-mica granites, muscovite granites, albite granites, and pegmatites, are widely exposed in the Lalong Dome [21]. Three types of rare metal mineralization have been identified in the Lalong Dome: skarn-type Be–Nb–Ta rare metal mineralization, albite granite-type Be–Nb–Ta rare metal mineralization and hydrothermal structure-type W–Cu–Pb–Zn polymetallic mineralization [22]. The first discovery of Lalong albite granite Be–Nb–Ta rare metal mineralization could play a significant role in building a better understanding of the relationship between leucogranites and rare metal mineralization in the Himalayan belt [23], which is the first large-scale albite granite-type Be–Nb–Ta deposit in the Himalayan metallogenic belt. It is further confirmed that the Himalayan metallogenic belt is a new rare metal metallogenic belt in China.

In this contribution, we carried out a detailed field observation and petrological, geochemical, and geochronological study of selected leucogranites—two-mica granites, muscovite granites, albite granites, and pegmatites—from the Lalong Dome. The objectives of this study are: (1) to constrain the timing of granitic magmatism and Be–Nb–Ta rare metal mineralization of the Lalong deposit for a comparison with the timing of other leucogranites and rare metal mineralization in the Tethyan Himalayan belt; (2) to ascertain the petrogenesis of the leucogranites in the Lalong Dome and provide evidence for the genesis of Himalayan leucogranites; (3) to elucidate the relationship between highly fractionated leucogranites and Nb–Ta–Be rare metal mineralization in the Lalong Dome; and (4) to point out the economic potential of rare metal leucogranites in the Tethyan Himalaya.

2. Regional Geology

The Himalayan collisional orogenic belt mainly consists of four tectonic units from north to south—the Tethys Himalayan Sedimentary Sequence (THS), the Higher Himalayan Crystalline Series (HHC), the Lesser Himalayan Sequence (LHS), and the Sub-Himalayan Sequence (SHS)—that are separated by five regional boundary fault systems toward the south: the Indus–Tsangpo suture zone (ITSZ), the South Tibetan detachment system (STDS), the Main Central Thrust (MCT), the Main Boundary Thrust (MBT), and the Main Frontal Thrust (MFT), respectively [24,25] (Figure 1A,B). The THS is mainly a set of Triassic–Cretaceous sedimentary rocks, including sandstone, siltstone, shale, and low-grade metamorphic slate and phyllite, and is characterized by the exposure of the North Himalayan Gneiss Domes (NHGDs), the east–west striking thrust faults, and north–south trending rifts (NSTRs) [26,27]. Most Pb–Zn and Au–Sb polymetallic deposits are controlled by the north–south trending faults in the THS, i.e., the large-scale Zhaxikang Pb–Zn polymetallic deposit [28–30].

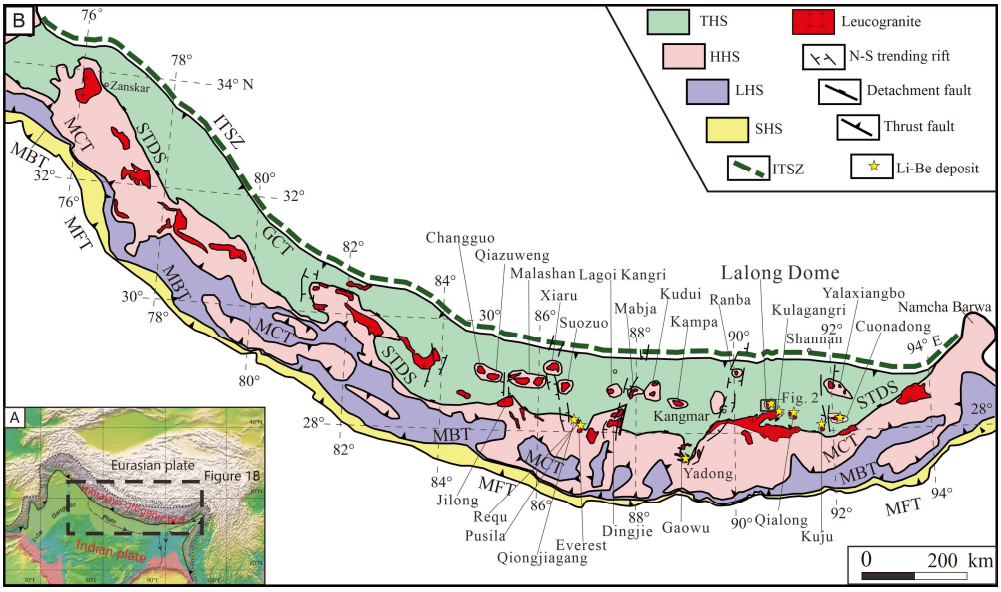

Figure 1. (**A**) Simplified geologic map of the Himalayan orogenic belt, showing the distribution of leucogranites and domes (modified from Wu et al., 2021 [19]). (**B**) ITSZ, Indus–Tsangpo Suture Zone; STDS, South Tibetan Detachment System; MCT, Main Central Thrust; MBT, Main Boundary Thrust; MFT, Main Frontal Thrust; THS, Tethyan Himalayan Sedimentary Sequence; HHS, Higher Himalayan Crystalline Series; LHS, Lesser Himalayan Sequence; SHS, Sub-Himalayan Sequence. Location of the Lalong Dome shown by rectangle in the eastern part.

The North Himalayan Gneiss Domes (NHGDs) are exposed between the ITSZ and the STDS [27,31–33] (Figure 1B). The NHGDs, from east to west, including Yalaxiangbo, Cuonadong, Kuju, Qialong, Kulagangri, Lalong, Ranba, Kangmar, Kampa, Mabja, Lagoi–Kangri, Malashan, and Jilong Dome (Figure 1B), generally show a similar geologic framework including a core of orthogneisses and leucogranites, a middle unit of high-grade metamorphic rocks, a and upper unit of lower grade–unmetamorphosed sedimentary rocks [27,31,34–37]. Although most of the domes underwent multiphase tectonic deformation, two typical structural deformations (D_1 and D_2) are always recorded in the NHGDs. D_1 is top-to-south thrust deformation. D_2 is top-to-north ductile shear deformation and crustal extension; this is interpreted as the result of a top-to-north detachment deformation of the STDS [26,31,34,38–44].

The Lalong Dome is located at the eastern part of the NHGDs (Figure 1A). In the south, the Lalong Dome is adjacent to the Kulagangri Dome which is the largest dome in the NHGDs, about 40 km away from the STDS, and the outcropping area is about 30 km^2.

3. Geology of the Lalong Dome

The Lalong Dome consists of three lithologic–tectonic units from the inner to outer: the lower unit (the core), and the middle and upper units (cover rocks) (Figure 2a,b, Figures 3 and 4A). The arc-shaped upper detachment fault is the boundary between the middle unit and upper unit, while the lower detachment fault is not well exposed in the Lalong Dome, which is characterized by the sheath fold around the core of the Lalong Dome. The lower unit consists of a set of the Cenozoic highly fractional crystallization leucogranites, from the core to the rim (Figure 3), including two-mica granite, muscovite granite, albite granite (Figure 4G), and pegmatite (Figure 4F,H,I). The Be–Nb–Ta rare metal ore bodies are mostly hosted by albite granite and pegmatite. The middle unit is commonly known as the detachment system, which has been interpreted as the northern part of the STDS [36,40]. Leucogranites in the lower unit partly intruded into the middle unit, and the boundary between the middle unit and lower unit is always serrated, irregular, and arc-shaped. The middle unit mainly consists of strongly deformed mica schist (Figure 4),

leucogranite, pegmatite, skarn (Figure 4D,E), and marble. The typical metamorphic minerals include kyanite, staurolite (Figure 4C), garnet, and biotite. The metamorphic grade decreases from core to rim, with a garnet + kyanite zone, a garnet + staurolite zone, and a biotite + garnet zone. These metasedimentary rocks in the middle unit preserve typical Barrovian peak metamorphism defined by mineral assemblages [22]. The skarn is dominated by calc-silicate minerals such as diopside, andradite and grossular. The main minerals in the skarns close to granite and pegmatite are quartz, albite, epidote, and calcite, which represent an internal skarn zone. Closer to the marble, the minerals comprise diopside, andradite–grossular, wollastonite, chlorite, actinolite, idocrase, phenacite, calcite, and fluorite, which represent an external skarn zone. The skarn-type Be–Na–Ta rare metal ore bodies are hosted by skarns in the middle unit of the Lalong Dome. On the other hand, albite granites and pegmatites in the middle unit of the dome are the lenticular and vein, with length ranging from 2 m to 200 m, and width from 1 m to 20 m. These albite granites and pegmatites are also the host rocks for the Be–Nb–Ta rare metal ore bodies. The upper unit, commonly known as the cover rocks, consists of phyllite, phyllitic slate (Figure 4B), and siltstone. The typical metamorphic minerals in this unit are cordierite, chloritoid (Figure 4B), and andalusite. The metamorphic grade within this unit decreases upsection from low metamorphic phyllite and phyllitic slate to unmetamorphosed sandstone and siltstone at the top.

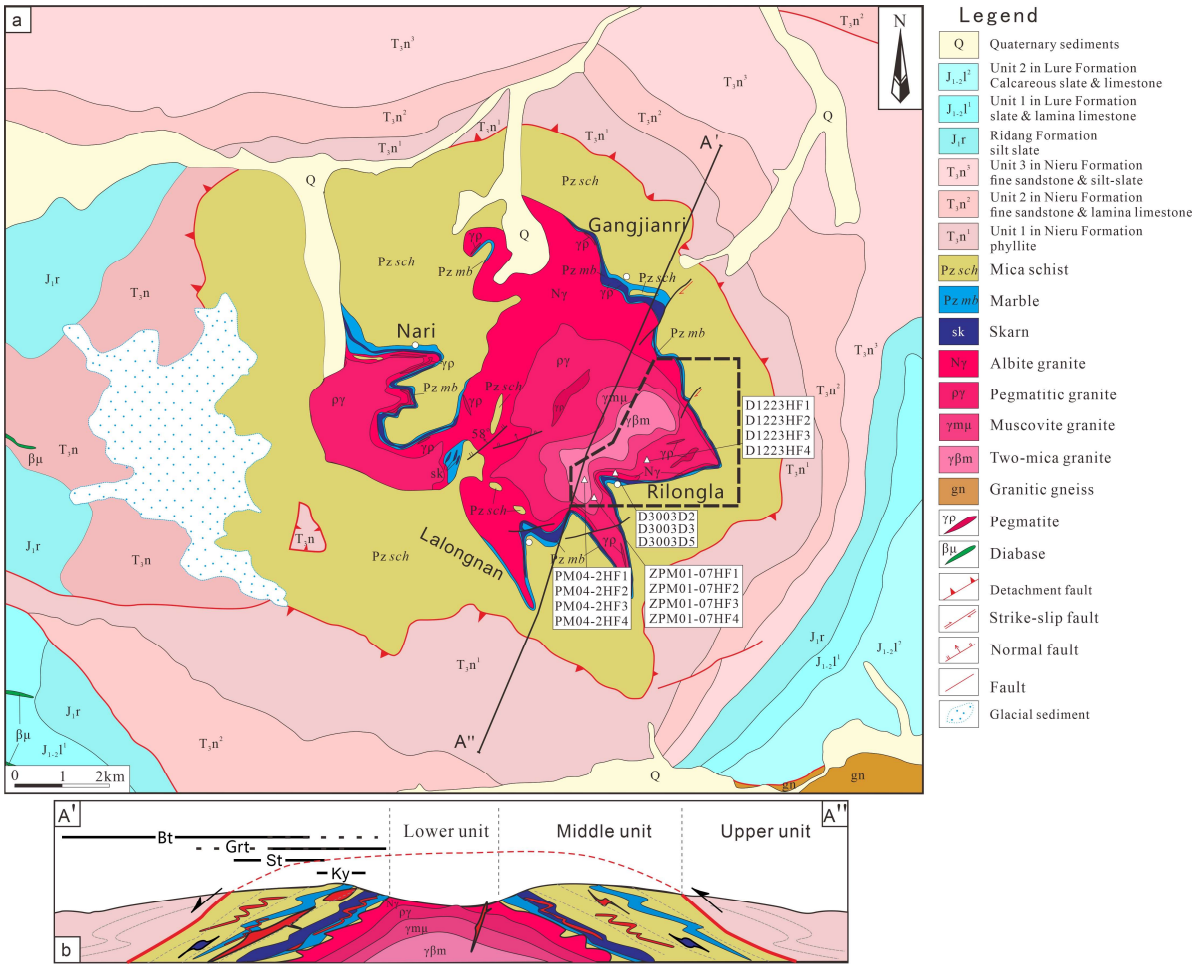

Figure 2. (**a**) Geological map of the Lalong Dome in Southern Tibet (modified from [22]). (**b**) Cross-section through the Lalong Dome (A′A″) with observed index metamorphic minerals (modified from [22]). Location of Figure 3 shown. Mineral abbreviation: Bt, biotite; Grt, garnet; St, staurolite; Ky, kyanite.

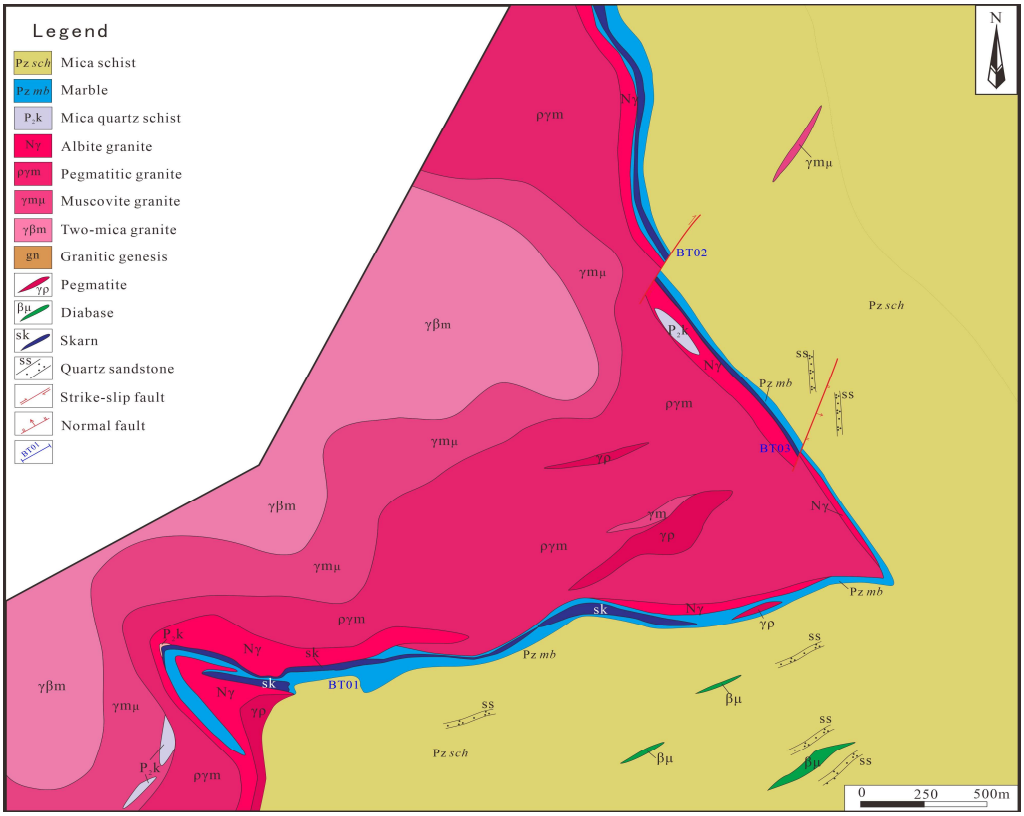

Figure 3. Geological map of the Rilongla Be–Nb–Ta rare metal target prospecting area in the Lalong Dome.

The Lalong Dome has experienced four major deformational events: D_1, top-to-S thrust; D_2, top-to-N shear characterized by vertical thinning and N–S extensional deformation; D_3, doming deformation associated with intrusion of leucogranites; and D_4, late extensional faults with N–S, E–W, and NE trending which also cut the above three units of the dome [22]. D_1 structures, as the Cenozoic oldest deformational event in the Lalong Dome, preserved in the middle and upper units. In the upper unit, the rocks are deformed by macroscopic, typically disharmonic F_1 folds and "M" or "W" type folds with the pervasive development of axial plane cleavage. In the middle unit, D_1 is characterized by S–C fabrics, the asymmetric fold, σ-type porphyroclast, and indicating top-to-S thrust shear sense. D_2, a relatively younger, high-strain deformational event, probably represents the residual northward detachment of the STDS. D_2 deformation in the Lalong Dome is characterized by penetrative foliation (S_2) and mineral stretching lineation (L_2). S_2 becomes an intensely developed mylonitic layer. Typical mylonite includes S–C fabrics, rotation structures in garnet, and sheath folds. In order to better distinguish from stretching lineation L_1, L_2 is predominantly defined by stretching lineation with the x-direction on the surface of the strongly deformed granite in the sheath folds. D_3 is always associated with the dome formation and is characterized by the intrusion of the latest albite granite. These granites partly intruded into the marble, skarn, and mica schist in the middle unit of the dome. D_4 is the latest brittle deformation event that probably resulted from the thermal cooling and gravitational collapse after the dome formation. These faults always crosscut all the older penetrative fabrics in the dome. The hydrothermal structure Cu–Pb–Zn mineralization in the Lalong Dome is controlled by the E–W and N–E trending faults.

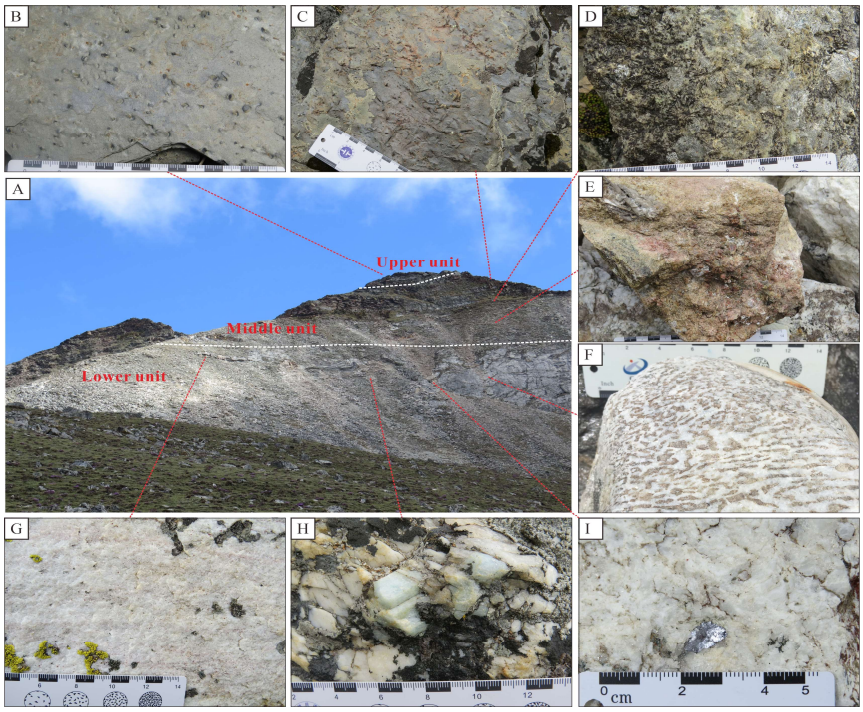

Figure 4. Field outcrop photos in the Lalong Dome in Southern Tibet. (**A**) Macrophotograph in the Rilongla Be–Nb–Ta rare metal target prospecting area in the Lalong Dome, showing three lithologic–tectonic units from the inner to outer: the lower unit (the core), middle, and the upper units (the cover rocks). (**B**) Cordierite-chloritoid-bearing slate in the upper unit of the Lalong Dome. (**C**) Garnet-staurolite-bearing mica schist in the middle unit. (**D**) Idocrase skarn in the middle unit. (**E**). Garnet idocrase skarn in the middle unit. (**F**) Pegmatite with graphic texture in the core of the Lalong Dome. (**G**) Fine-grained albite granite in the core. (**H**) Beryl-bearing pegmatite in the core. (**I**) Molybdenite-bearing pegmatite in the core.

There are three types of mineralization in the Lalong Dome: albite granite-type Be–Nb–Ta rare metal mineralization, skarn-type Be–Nb–Ta rare metal mineralization, and hydrothermal structure-type W–Pb–Zn polymetallic mineralization [22]. Albite granite-type Be–Nb–Ta rare metal mineralization is the focus of this contribution, and the other two types of mineralization will be reported in other papers. Lalong albite granite-type Be–Nb–Ta rare metal mineralization is mainly hosted by albite granite and pegmatite. The controlled strike length of the rare metal ore bodies is ca. 1500 m. The average thickness of orebody is 5 m, the average grades of BeO, Rb_2O, Nb_2O_5, and Ta_2O_5 are 0.0785%, 0.0556%, 0.0087%, 0.0208%, respectively. The ore structure is generally a massive structure, and the ore texture is mostly euhedral–granular and metasomatic. The main rare metal minerals are columbite, tantalite, pyrochlore, teshirogilite, tapiolite, beryl (Figure 4H), uraninite, microlite, Nb–Ta-bearing rutile, and fergusonite. In addition, molybdenite (Figure 4I) is mainly scattered in pegmatite. The main gangue minerals are quartz, albite, K-feldspar, muscovite, with minor garnet, tourmaline, and biotite. Both the albitization and greisenization occur in the Lalong albite granite-type rare metal deposit.

4. Sample Petrology

Leucogranites, exposed in the core of the Lalong Dome, include four types from the core to rim: (1) two-mica granite, (2) muscovite granite, (3) albite granite, and (4) pegmatite. These show good lithofacies zoning (Figures 2a and 3). The sampling locations in this contribution are shown in Figure 2. Two-mica granite generally occurs at the core of the dome, and comprises gray–in–hand specimens (Figure 5A). Two-mica granite is primarily medium–fine-grained and typically consists of quartz, plagioclase, K-feldspar, muscovite, biotite, garnet, tourmaline, and accessory zircon, monazite, and apatite (Figure 6A). Plagio-

clase commonly occurs as euhedral to subhedral laths. The K-feldspar is often characterized by subhedral and anhedral habits. Most muscovite grains are in textual equilibrium with the other phases, suggesting that this muscovite is the primary mineral. The quartz grains are normally anhedral and are distributed between other mineral crystals.

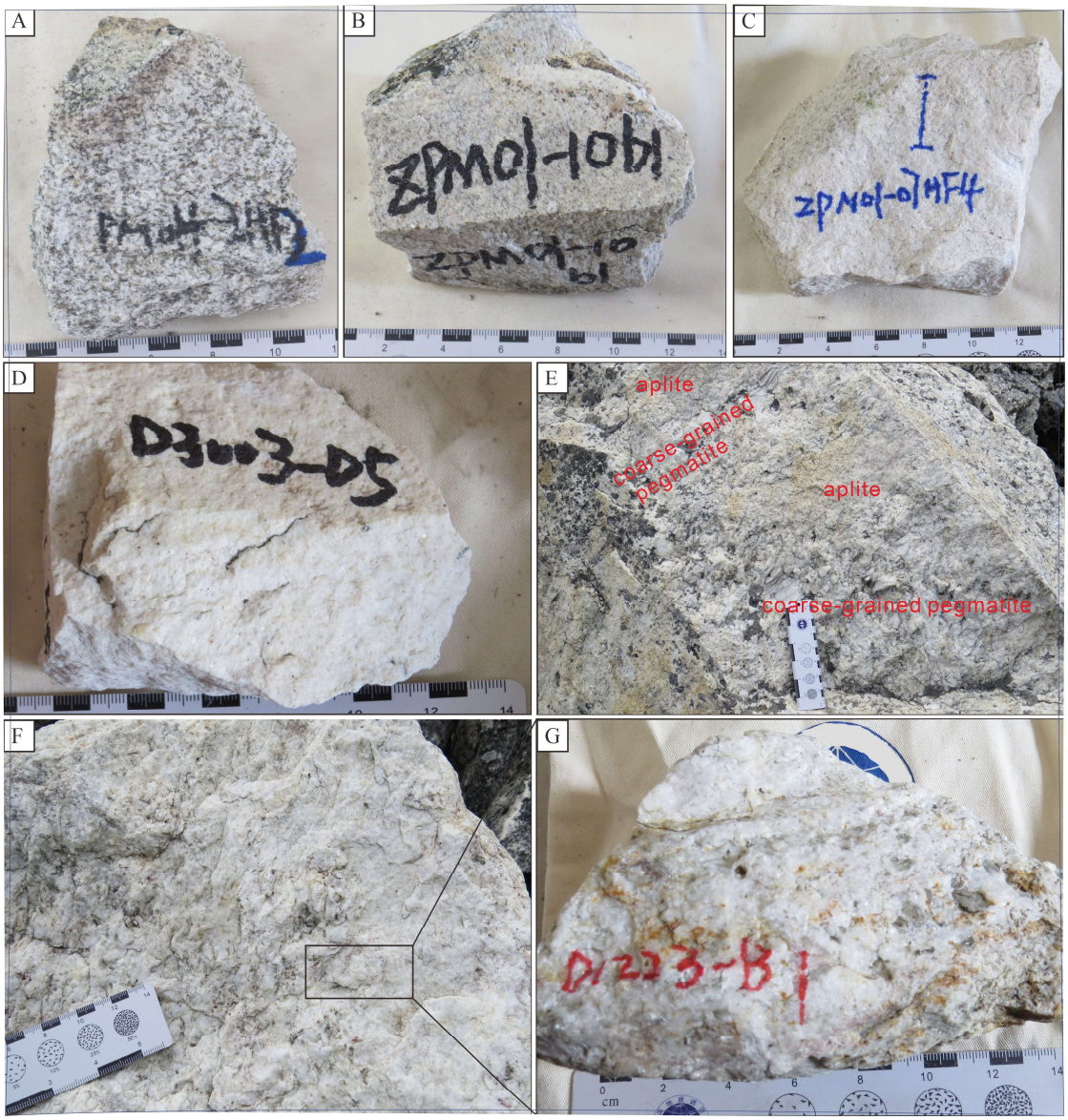

Figure 5. Photos of hand specimen samples in the Lalong Dome. (**A**) Two-mica granite in the core. (**B**) Muscovite granite in the core. (**C**) Albite granite in the core. (**D**) Albite granite in the core. (**E**) Pegmatite, including coarse-grained pegmatite and aplite in the core. (**F**,**G**) Pegmatite. The numbers and letters on the sample surface are the sample number.

Muscovite granite is widely exposed in the core of the dome, some of which are independent veins, and the contact boundary with pegmatite is obvious. Some of them are surrounded by pegmatite, and the boundaries are blurred and gradual. In the outcrop, two-mica granite and muscovite granite show a gradual transition relationship, and the boundary is not very clear. Muscovite granite is primarily medium–fine grained, and is light gray in color in hand specimens (Figure 5B). The main minerals in muscovite granite are quartz, plagioclase, K-feldspar, muscovite, garnet (Figure 6B,C) and a small amount of tourmaline and biotite, and the secondary minerals are zircon, monazite, apatite, phosphtrium, and columbite group mineral (CGM). The garnet crystals occur as purple–

pink euhedral crystals that are as big as 1–3 mm in diameter and are free of inclusions (Figure 6B). The results of electron probe analysis show that garnet in muscovite granite is mainly almandite [21].

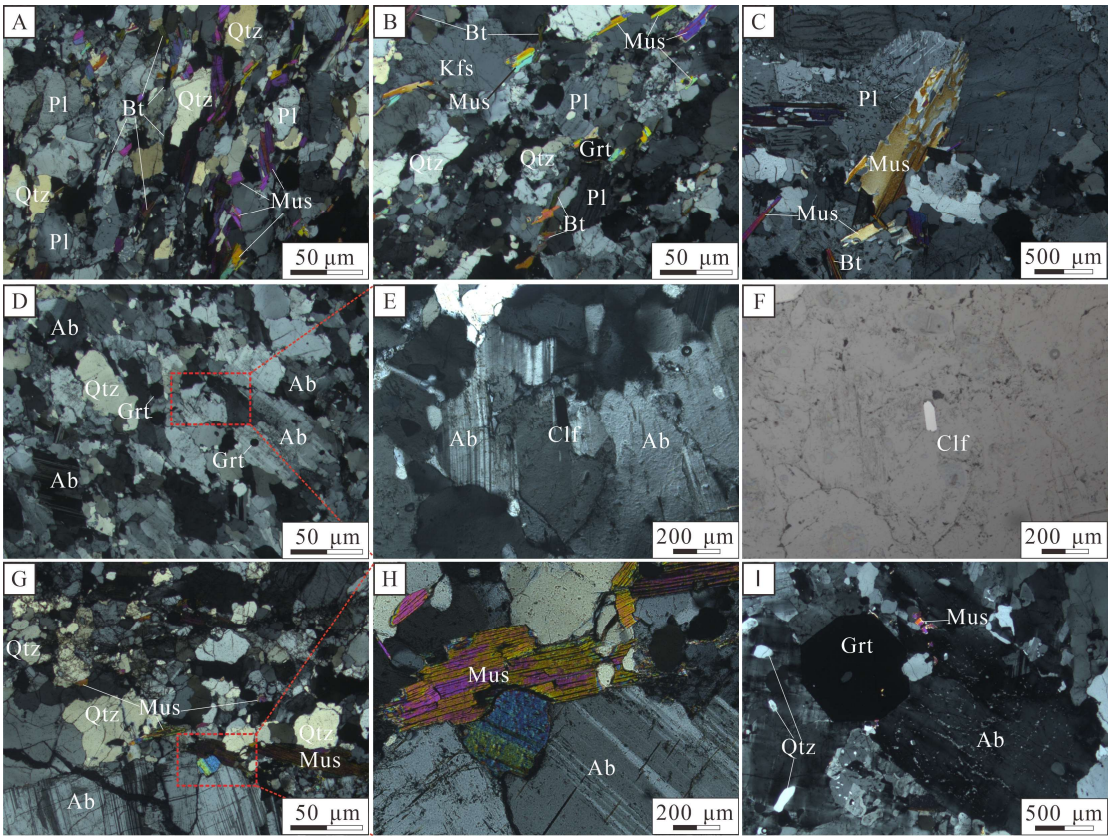

Figure 6. Photomicrographs of leucogranite samples in the Lalong Dome. (**A**) Photomicrograph of two-mica granite in cross-polarized light. (**B**) Photomicrograph of muscovite granite in cross-polarized light. (**C**) Photomicrograph of muscovite granite in cross-polarized light. (**D**,**E**) Photomicrograph of albite granite in cross-polarized light. (**F**) Photomicrograph of albite granite in plane-polarized light, showing columbite in albite. (**G**,**H**) Photomicrograph of pegmatite in cross-polarized light. (**I**) Photomicrograph of pegmatite in cross-polarized light, showing quartz inclusions in albite and representing fluid dissolution. Mineral abbreviation: Ab, albite; Kfs, K-feldspar; Pl, plagioclase; Qtz, quartz; Mus, muscovite; Bt, biotite; Grt, garnet; Clf, columbite.

Albite granite is mostly distributed in the edge of the core, and is named as a-type albite granite. Some of it intrudes into the marble and skarn in the middle unit, and either parallel to or cutting through the marble bedding, these albite granites are named as b-type albite granite. In the outcrop, albite granite and muscovite granite also show a gradual transition relationship, and the boundary is not very clear. Albite granite is predominately fine grained and sugar-granular in texture, and is white or creamy white on outcrop or hand specimens (Figure 5C,D). Albite granite is mainly composed of minerals with albite, quartz, white mica, garnet, and a small amount of K-feldspar and tourmaline (Figure 6D,E), as well as accessory zircon, monazite, apatite, phosphtrium and columbite group mineral (CGM) (Figure 6E,F), uraninite, and pyrochlore. Albite is characterized by a sugar-granular and foliated lamellar texture (Figure 5C,D). The garnet crystals occur as pink euhedral crystals that are as much as 0.5–3 mm in diameter and are also free of inclusions (Figure 6D). Garnet in albite granite is predominantly spessartite [21]. Muscovite grains are fine-grained and scaly.

Pegmatites are widely exposed in the core of the dome, some of them are independent dikes, some of them intrude or interpenetrate into the two-mica granite and muscovite

granite, and some of them are distributed along the edge of the core of the dome. Pegmatite mainly consists of plagioclase, quartz, muscovite, tourmaline, garnet, beryl, and accessory Nb–Ta–(Ti) oxide minerals, zircon, monazite, and apatite. Pegmatite is mainly distributed in the core of the dome near the edge, and overall is in the shape of oats on the outcrop or hand specimens (Figure 5E,F). Pegmatite is characterized by the complex internal structure including the coarse-grained pegmatite and aplite (Figure 5E). The boundary between coarse-grained pegmatite and aplite is very fuzzy, showing a gradual transition relationship. Pegmatite is mainly composed of albite, K-feldspar, quartz, muscovite, garnet and a small amount of tourmaline (Figure 6G–I), as well as accessory zircon, monazite, apatite, phosphtrium and columbite group mineral (CGM), uraninite, and pyrochlore. The mineral grains in the coarse-grained pegmatite range from 3 cm to 10 cm.

5. Methodology

5.1. Monazite U–Th–Pb and Columbite U–Pb Dating

In order to constrain the timing of granitic magmatism in the Lalong Dome, three representative samples including two-mica granite sample PM04-2TW, albite granite sample D3003D1, and pegmatite sample D1223-TW1 are selected for monazite U–Th–Pb dating. Three leucogranite samples from the Lalong Dome were selected for monazite U–Th–Pb geochronology: two-mica granite sample PM04-2TW, albite granite sample D3003D1, and pegmatite sample D1223-TW1. Albite granite sample D3003D1 was also collected for columbite U–Pb dating.

The entire analyses were performed at State Key Laboratory of Metallogenic Mechanism of Endogenous Metal Deposits, Nanjing University, China. Using a combination of back-scattered electron (BSE) images and optical microscopy, the clearest, least fractured rims of the monazite and CGM crystals were selected as suitable targets for laser ablation inductively coupled plasma mass spectrometry (LA-ICPMS) analysis. The laser denudation injection system was a Resolution S-155 193 nm ArF excimer laser from ASI (Australia), coupled with an iCAP Q quadrupole plasma mass spectrometer from Thermo Fisher Scientific (Waltham, MA, USA).

The conditions for monazite U–Pb isotopic dating and trace element analysis are as follows: laser denudation spot diameter was 20 μm; the energy density was ~3 J/cm^2; and the frequency was 3 Hz. Analytical dwell time was set at 10 ms for ^{232}Th and ^{238}U, 15 ms for ^{204}Pb, ^{206}Pb and ^{208}Pb, 20 ms for ^{207}Pb, and 7 ms for all other elements. Every eight sample analyses were followed by analysis of the monazite standards (Treblicock, M4) and two standard glass NIST 610 and NIST 612. Monazite standard Treblicock (TIMS age 272 ± 2 Ma, Tomascak et al., 1996) was used to correct U–Pb isotope fractionation.

Detailed analysis procedures for CGM U–Pb isotope dating can be found in [45]. The conditions for columbite U–Pb isotopic dating are that the laser denudation spot diameter was 43 μm, an energy density of ~5 J/cm^2, and a frequency of 4 Hz. The dwell times of the analyzed elements were 10 ms for ^{232}Th and ^{238}U, 15 ms for ^{204}Pb, ^{206}Pb and ^{208}Pb, 30 ms for ^{207}Pb, and 6 ms for all other elements. Every eight sample analyses were followed by analysis of the tantalite standards (Coltan139) and four standard glass samples including two standard glass NIST 610, one USGS standard glass BCR-2G, and one USGS standard glass GSE-1G. Tantalite sample Coltan139 (TIMS age 505 ± 3.4 Ma, Gerdes) was used to correct U–Pb isotope fractionation.

In the Monazite U–Th–Pb and columbite U–Pb analyses, the analysis time of each sample point was 90 s, in which the background signal was collected for 20 s, the sample signal was collected for 50 s, and the cleaning time was 20 s. Data reduction was performed using the GLITTER (v. 4.0) program [46]. Isoplot V4.15 software was used to plot the concordia diagram and calculate the weighted average age [47]. Results of isotopic measurement on monazite and columbite are listed in Tables S1 and S2, respectively.

5.2. Whole-Rock Geochemical Analysis

Fresh samples (each one weights about 2 kg) were selected for major- and trace-element analysis. Samples were crushed initially in a jaw crusher. Analysis of major and trace elements was conducted at Shandong Bureau Test Center, China Metallurgical Geology General Administration. Major elements were determined using X-ray fluorescence spectrometry (XRF) with relative standard deviations within 5% using standard fused-bead and pressed-pellet technique. The loss on ignition (LOI) was determined by a pre-ignition method before major element analyses. Trace elements, including the rare earth elements (REE) and high field strength elements (HFSE), were analyzed using inductively coupled mass spectrometry (ICPMS) following HF–HNO_3–$HClO_4$ acid digestion and HCl leach. The analytical precisions for major elements were 1%–3% (for those present at concentrations of higher than 1%) and approximately 5% (for those with concentrations of less than 1%). The analytical uncertainties for the trace elements were 10% (for those with abundances of less than 10 ppm) and approximately 5% (for those with concentrations of more than 10 ppm). The analysis results are presented in Table S3.

5.3. Sr and Nd Isotope Analysis

To determine Sr and Nd isotopes, nine leucogranite samples were selected (the least-altered samples), crushed, and ground in an agate ring mill. All the analytical procedures were analyzed by the micromass isoprobe multi-collector inductively coupled plasma mass spectrometer (MC-ICPMS) at National Geological Experiment and Test Center (Beijing, China). The main analysis process is as follows: accurately weigh 0.25 g powder sample, and then put them into the Teflon stew tank, add 0.5 mL HNO_3 and 1.5 mL HF, close and heat digestion at 190 °C for 48 h, remove HF at 160 °C, add 3 mL 1:1 HNO_3, close and redissolve at 150 °C for 6 h, and constant volume to 25 g. According to the Nd content, appropriate sample solution was centrifuged, the supernatant was dried, and the acidity was adjusted. LN special resin was used to separate pure Nd, and the sample solution containing Nd was obtained. $^{143}Nd/^{144}Nd$ values were determined using a Thermo Fisher Scientific multi-receiver inductively coupled plasma mass spectrometer Neptune Plus MC-ICPMS. According to the natural abundance ratio of $^{146}Nd/^{144}Nd$ (0.7218), the measured $^{143}Nd/^{144}Nd$ values were corrected by online mass fractionation according to the exponential law. The uncertainty of $^{143}Nd/^{144}Nd$ value is 2σ, which only includes the uncertainty determined by mass spectrometry. The analytical data and calculated results are listed in Table S4.

6. Results

6.1. Monazite U–Th–Pb Dating

Monazite grains from the leucogranite are light yellow, subhedral–euhedral, mainly short columnar and granular, with length ranging from 60 μm to 150 μm. These monazites generally have no distinct zoning under BSE images. Twenty-four U–Pb analyses in two-mica granite sample PM04-2TW were performed using LA-ICPMS method. From sample PM04-2TW, 23 analysis spots yielded a weighted-mean of $^{208}Pb/^{232}Th$ age of 23.6 ± 0.1 Ma (1σ; MSWD = 1.1; n = 24) (Figure 7A,B). Twenty-four U–Pb analyses in albite granite sample D3003D1 were performed, and nineteen analysis spots from sample D3003D1 yielded a weighted-mean $^{208}Pb/^{232}Th$ age of 21.9 ± 0.1 Ma (1σ; MSWD = 0.49; n = 19) (Figure 7C,D). Twenty-five U–Pb analyses in pegmatite sample D1223-TW1 were performed, and twenty-five analysis spots from sample D1223-TW1 yielded a weighted-mean of $^{208}Pb/^{232}Th$ age of 20.6 ± 0.1 Ma (1σ; MSWD = 1.8; n = 25) (Figure 7E,F).

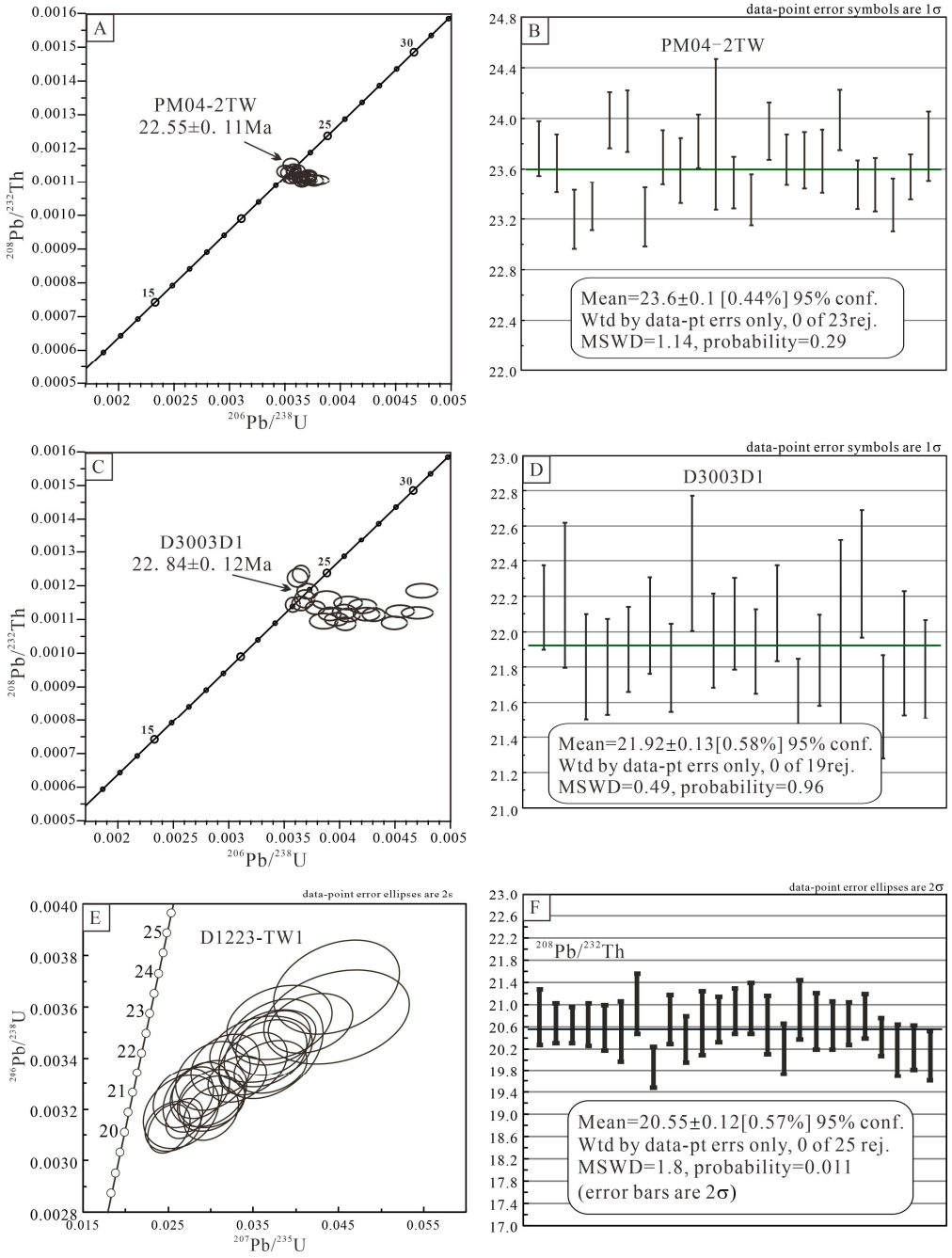

Figure 7. U–(Th)–Pb dating results of the leucogranites in the Lalong Dome. (**A**) LA–ICP–MS monazite U–Th–Pb dating results of two-mica granite. (**B**) Weighted average age dating diagram of two-mica granite. (**C**) LA–ICP–MS monazite U–Th–Pb dating results of albite granite. (**D**) Weighted average age dating diagram of albite granite. (**E**) LA–ICP–MS monazite U–Th–Pb dating results of pegmatite. (**F**) Weighted average age dating diagram of pegmatite.

6.2. Columbite U–Pb Dating

To better constrain for Be–Nb–Ta mineralization of the Lalong deposit, a representative albite granite sample D3003D1 is selected for columbite U–Pb dating. Sample D3003D1 contains subhedral to euhedral CGM grains with lengths ranging from 150 μm to 600 μm that display the typical zoning and complex structures (Figure 8A). The clear oscillatory zoning and complex structures are usually formed in the magmatic stage and the magma–hydrothermal transition stage. Twenty-five U–Pb analyses in albite granite sample D3003D1 were performed, and twenty-one analysis spots from sample D3003D1 yielded a concordant

of $^{206}Pb/^{238}U$ age of 21.5 ± 0.9 Ma (1σ; MSWD = 2.2; *n* = 21) (Figure 8B) and a weighted-mean of $^{206}Pb/^{238}U$ age of 20.9 ± 0.5 Ma (1σ; MSWD = 2.3; *n* = 21) (Figure 8C).

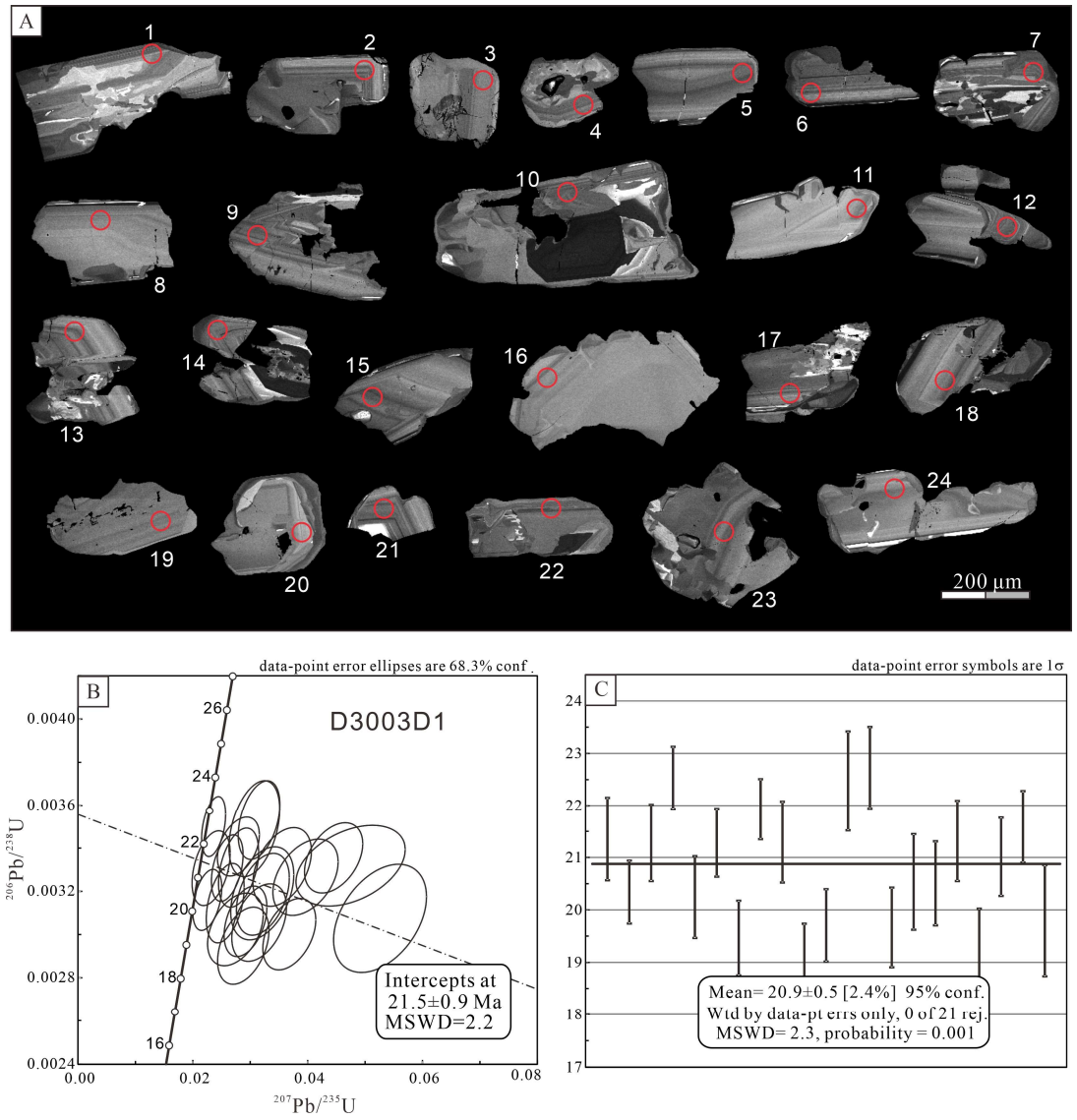

Figure 8. (**A**) Back-scattered electron (BSE) images of the analysed CGM grains in albite granite sample D3003D1. The red circle and number represent the analysis point and spot, respectively. (**B**) U–Pb concordia diagrams for CGM sample. (**C**) Weighted average age dating diagram.

6.3. Major and Trace Element Compositions

The leucogranite samples in the Lalong Dome fall in the granite field in the TAS classification plot (Figure 9A). Two-mica granites, muscovite granites, albite granites, and pegmatites have high SiO_2 contents of 73.1–74.7 wt.%, 73.6–74.2 wt.%, 73.3–74.8 wt.%, and 74.8–76.6 wt.%, respectively. These leucogranitic rocks are peraluminous (Figure 9B) with high Al_2O_3 content (13.6–15.2 wt.%) and A/CNK [molar $Al_2O_3/(CaO + Na_2O + K_2O)$] (1.02–1.2). Two-mica granites and muscovite granites are characterized by the high-K calc-alkaline series, while albite granites, and pegmatites are calc-alkaline series (Figure 9C). In the Hark diagrams (Figure 10), Na_2O content from two-mica granites, muscovite granites to albite granites and pegmatites are gradually increasing with the SiO_2 content. MgO, CaO, Al_2O_3, TiO_2, and P_2O_5 content from two-mica granites, muscovite granites–albite granites, and pegmatites gradually decrease with the SiO_2 content increase.

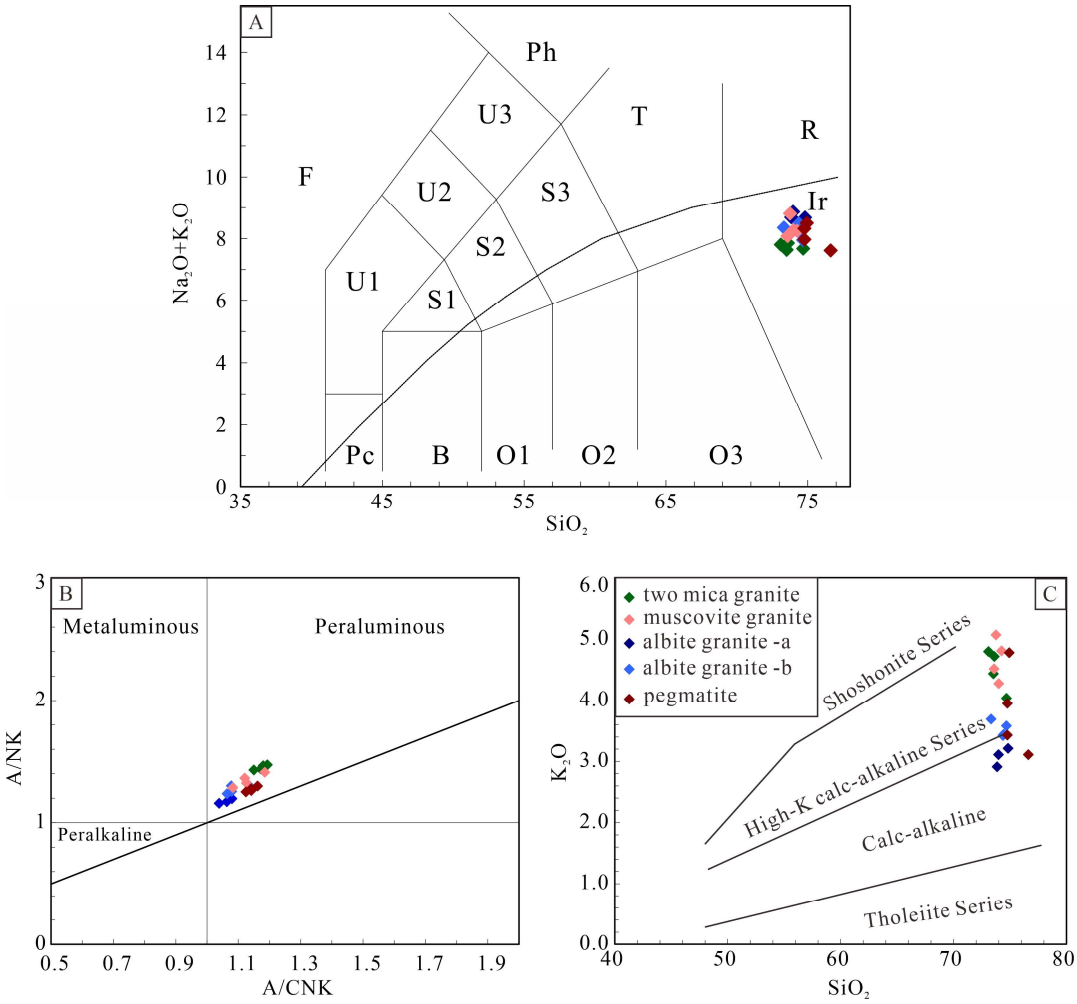

Figure 9. (**A**) TAS diagram [48] for leucogranites from the Lalong Dome. Pc, Peridotgabbro; B, Gabbro; O1, Gabbroic Diorite; O2, Djorite; O3, Granodiorite; U1, Foid Gabbro; U2, Foid Monzodiorite; U3, Foid Monzosyenite; Ph, Foid Syenite; S1, Monzogabbro; S2, Monzodiorite; S3, Monzonite; Ir, Granite; F, Foidolite. (**B**) Shand's index Al/(Na + K) versus Al/(Ca + Na + K) plot [49]. (**C**) K_2O versus SiO_2 diagram [50].

In general, the Lalong leucogranites are enriched in highly incompatible trace elements (LILEs) and depleted in high-field-strength elements (HFSEs). In the primitive mantle-normalized spider grams (Figure 11), leucogranites exhibit similar patterns, and are depleted in Ba, Sr, Zr, and Ti, but enriched in Rb, Pb, Nb, and Ta. Furthermore, their REEs show similar patterns in the chondrite-normalized patterns, featured by negative anomalies of Eu with obvious negative Eu anomalie in albite granites and pegmatites. The term "tetrad effect" refers to the subdivision of the 15 lanthanide elements into four groups in a REE chondrite-normalized distribution pattern: (1) La–Ce–Pr–Nd, (2) Pm–Sm–Eu–Gd, (3) Gd–Tb–Dy–Ho, and (4) Er–Tm–Yb–Lu [51]. The existence of the "tetrad effect" in highly evolved peraluminous magmatic systems is the result of the interaction between the melt and the phase containing volatilization diverge, which is the criterion of the degree of magma differentiation. Albite granites and pegmatites exhibit a significant lanthanide tetrad effect which is confined by the degree of the tetrad effect ($TE_{1,3}$) that ranges from 1.11 to 1.33. $TE_{1,3}$ is defined as $(TE_1 \times TE_3)^{0.5}$, $TE_1 = (Ce/Ce^* \times Pr/Pr^*)^{0.5}$, $TE_3 = (Tb/Tb^* \times Dy/Dy^*)^{0.5}$, $Ce^* = La_N^{2/3} \times Nd_N^{1/3}$, $Pr^* = La_N^{1/3} \times Nd_N^{2/3}$, $Tb^* = Gd_N^{2/3} \times Ho_N^{1/3}$, $Dy^* = Gd_N^{1/3} \times Ho_N^{2/3}$; the subscript N is chondrite-normalized lanthanide concentration [52].

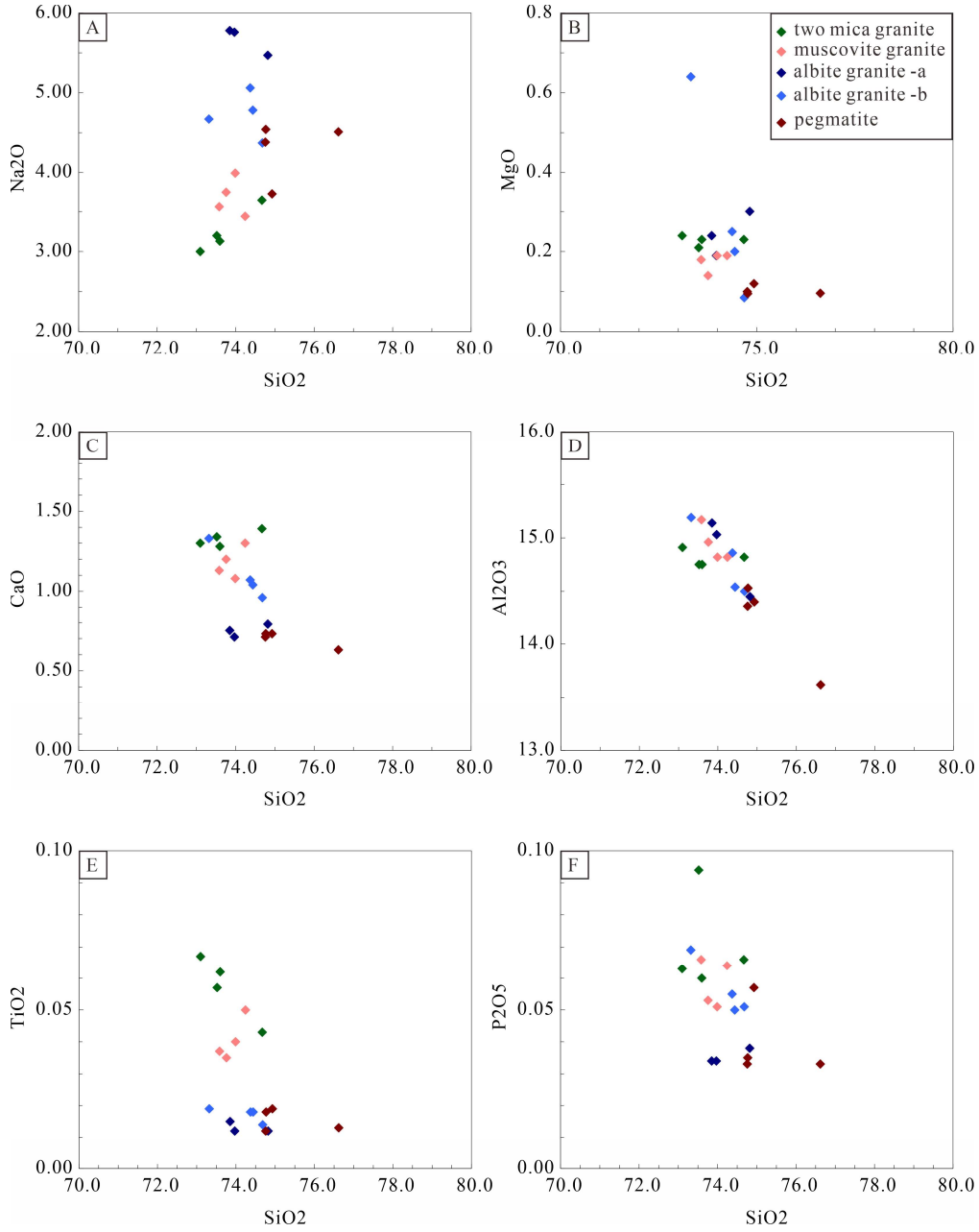

Figure 10. Harker variation diagrams for major elements. (**A**) SiO_2 vs. Na_2O diagram. (**B**) SiO_2 vs. MgO diagram. (**C**) SiO_2 vs. CaO diagram. (**D**) SiO_2 vs. Al_2O_3 diagram. (**E**) SiO_2 vs. TiO_2 diagram. (**F**) SiO_2 vs. P_2O_5 diagram.

Two-mica granites have the highest total REE concentration (71.4–93.8 ppm) and highest Nb/Ta (12.21–19.41), Zr/Hf ratios (19.14–22.73), and the lowest $TE_{1,3}$ values (1.06–1.07). Muscovite granites have higher total REE content (71.9–87.7 ppm) and higher Nb/Ta (4.07–8.67), Zr/Hf ratios (15.87–19.3), and lower $TE_{1,3}$ values (1.09–1.21). The a-type albite granites have lower total REE content (36.3–56.3 ppm) and lower Nb/Ta (3.63–5.77), Zr/Hf ratios (10.43–10.56), and lower $TE_{1,3}$ values (1.22–1.26), while b-type albite granites with Nb/Ta (11.42–20.63), Zr/Hf ratios (14.37–15.28), and lower $TE_{1,3}$ values (1.11–1.15). Pegmatites have Nb/Ta (2.14–4.19), Zr/Hf ratios (8.26–9.32), and lower $TE_{1,3}$ values (1.26–1.33).

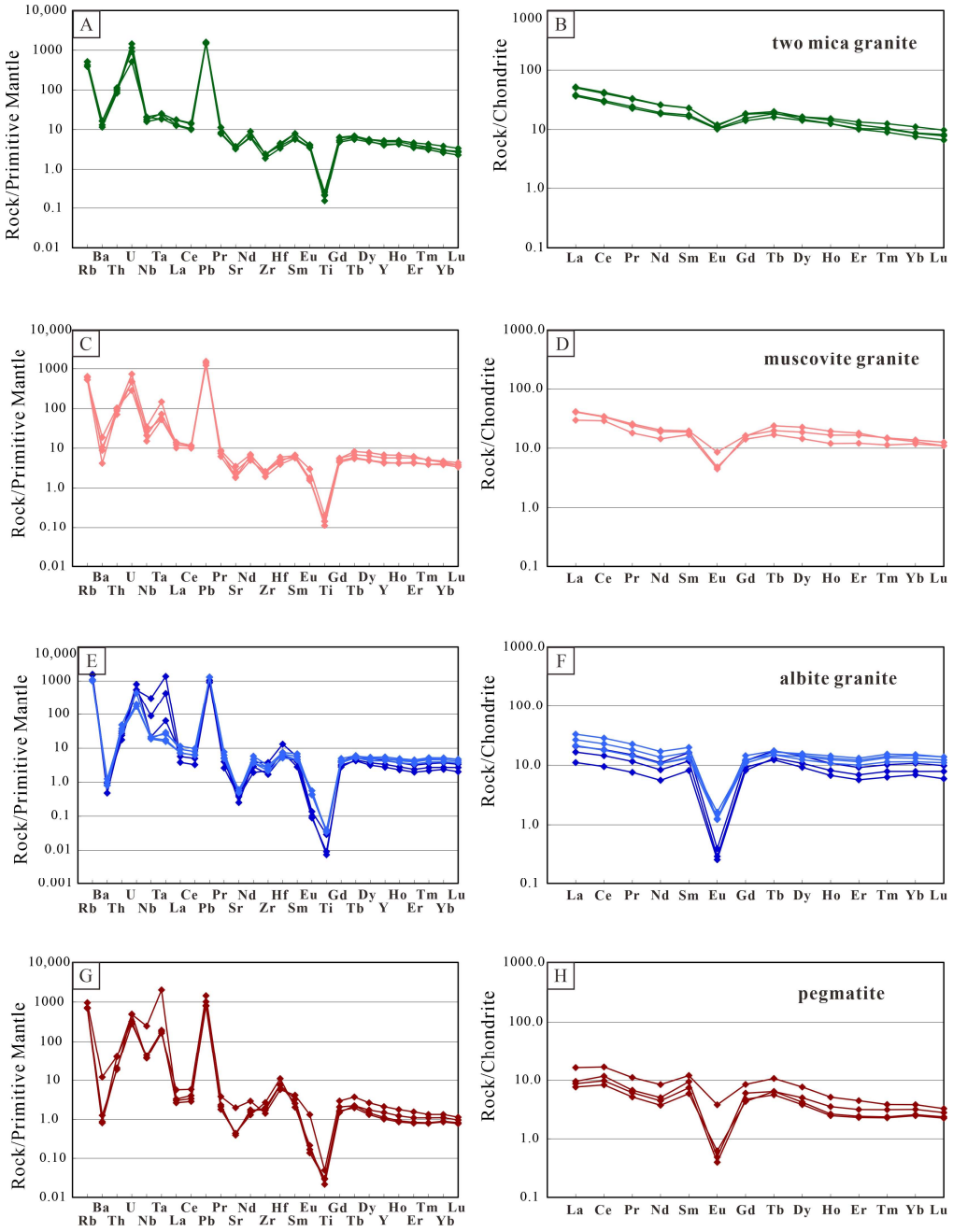

Figure 11. Primitive mantle-normalized spider diagrams (**A**,**C**,**E**,**G**) and chondrite-normalized REE patterns (**B**,**D**,**F**,**H**) for leucogranites in the Lalong Dome, respectively.

6.4. Whole-Rock Sr–Nd Isotopes

Two-mica granites from the Lalong Dome have Rb content ranging from 320 to 329 ppm and Sr content ranging 69.7 to 75.5 ppm, with $^{87}Rb/^{86}Sr$ ratios ranging from 12.6 to 13.3. These granites have $^{87}Sr/^{86}Sr(i)$ ratios [$^{87}Sr/^{86}Sr(i) = {}^{87}Sr/^{86}Sr + {}^{87}Rb/^{86}Sr(e^{\lambda t} - 1)$] that range from 0.736524 to 0.736548, $^{143}Nd/^{144}Nd$ ratios range from 0.511985 to 0.512014, and $\varepsilon Nd(t)$ values range from −12.69 to −12.10.

Muscovite granites have Rb content ranging from 335 to 407 ppm and Sr content ranging 38.2 to 39.7 ppm, with $^{87}Rb/^{86}Sr$ ratios ranging from 25.5 to 29.8. They have $^{87}Sr/^{86}Sr(i)$ ratios that range from 0.737010 to 0.739400, $^{143}Nd/^{144}Nd$ ratios range from 0.511987 to 0.512092, and $\varepsilon Nd(t)$ values that range from −12.70 to −10.76.

The a-type albite granites have Rb content ranging from 954 to 956 ppm and Sr content ranging 7.97 to 8.77 ppm, with $^{87}Rb/^{86}Sr$ ratios ranging from 317.6 to 349. They have $^{87}Sr/^{86}Sr(i)$ ratios that range from 0.673811 to 0.67671, $^{143}Nd/^{144}Nd$ ratios range from 0.512033 to 0.512049, and εNd(t) values range from −12.06 to −11.76. The b-type albite granites have Rb content of 626 ppm and Sr content of 10.3 ppm, with $^{87}Rb/^{86}Sr$ ratio of 176.8. They have $^{87}Sr/^{86}Sr(i)$ ratio of 0.710205, $^{143}Nd/^{144}Nd$ ratio of 0.512005, and εNd(t) value of −12.45.

Pegmatites have Rb content ranging from 441 to 445 ppm and Sr content ranging 8.27 to 9.11 ppm, with $^{87}Rb/^{86}Sr$ ratios ranging from 142.1 to 155.2. they have $^{87}Sr/^{86}Sr(i)$ ratios that range from 0.715228 to 0.718533, $^{143}Nd/^{144}Nd$ ratios range from 0.512143 to 0.512162, and εNd(t) values range from −10.04 to −9.77. εNd(t) values were calculated at 23 Ma. Sr–Nd isotopic data are shown in Table S4, and plotted in Figure 12.

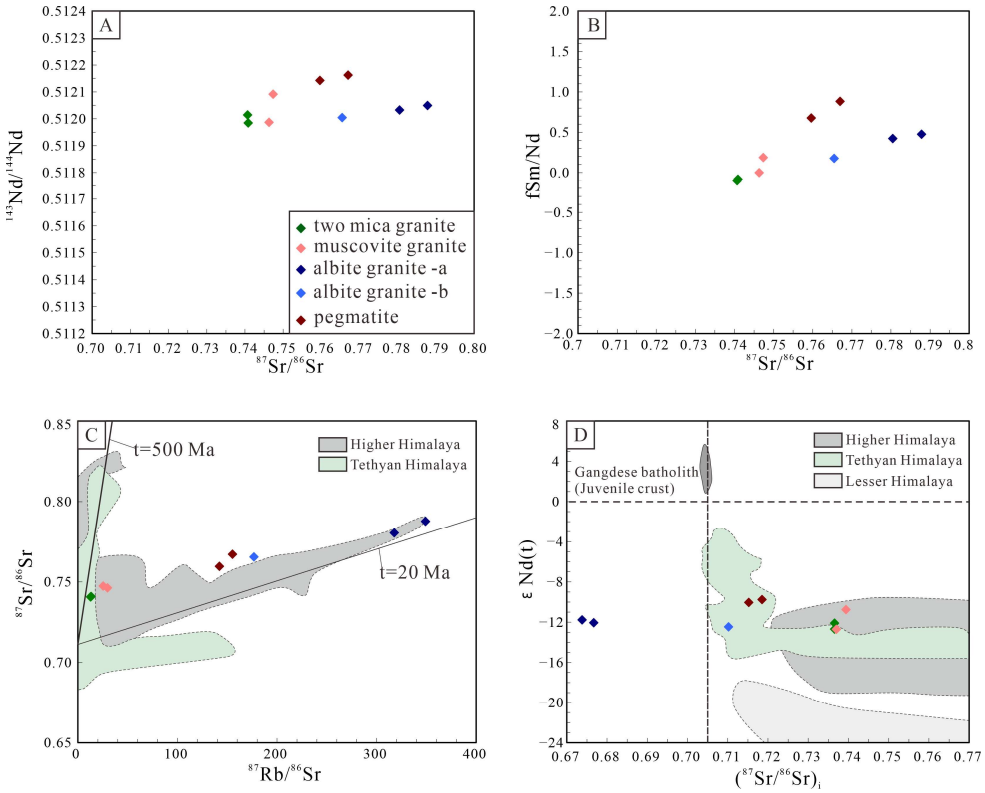

Figure 12. (**A**) $^{143}Nd/^{144}Nd$ vs. $^{87}Sr/^{86}Sr$ diagram. (**B**) $f_{Sm/Nd}$ vs. $^{87}Sr/^{86}Sr$ diagram. (**C**) $^{87}Sr/^{86}Sr$ vs. $^{87}Rb/^{86}Sr$ diagram. (**D**) $\varepsilon_{Nd}(t)$ vs. $(^{87}Sr/^{86}Sr)_i$ diagram. Regional data are from Wu et al. (2020) [8].

7. Discussion

7.1. The Emplacement Age of Leucogranites and Timing of Nb–Ta–Be Rare Metal Mineralization in the Lalong Dome

Leucogranites are widely exposed in the Tethys Himalayan Sedimentary Sequence (THS), which mostly controlled by the dome structure [9]. A lot of geochronological studies have been carried out on the leucogranites in the northern Himalaya, especially in the NHGDs. The emplacement ages of these granites are mainly concentrated in Oligocene–Miocene, and some Eocene granites are found, such as granites of about 45–44 Ma in the Yalaxiangbo Dome [53] and the Ranba Dome [13], and granites of 37 Ma in the Dingri Dome. At the same time, ca. 508 Ma granites are reported in the Kangmar Dome [54], which is consistent with the crystallization age of granitic gneiss in other domes (e.g., 500 Ma granitic gneiss in Cuonadong Dome) [43]. The emplacement age of Oligocene–Miocene leucogranite in the NHGDs is basically interpreted as the active timing of the STDS, and its initial initiation time is about 35 Ma at the earliest [43,55]. The termination age of the STDS was determined by the mica Ar–Ar age, which was about 14 Ma, indicating that the duration

of the STDS activity was about 21 Ma [16,31,43]. The STDSs, which are continuously active for a long time, are also accompanied by multiple periods of magmatic activity, with at least two or three periods of magmatic activity in each dome in the NHGDs. For example, the Yalaxiangbo Dome records three periods of magmatic activity since Eocene, ranging from old to new, these are 45.4 Ma, 35.3 Ma, and 20.2 Ma, respectively [53]. The Ranba Dome also records three periods of magmatic activity, 44.3 Ma, 28.0 Ma, and 7.6 Ma, respectively, from old to new [13]. Three periods of magmatic activity were recorded in the Jilong area: 27.0 Ma, 20.0 Ma, and 16.8 Ma. Three periods of magmatic activity (23.2 Ma, 15.8 Ma, and 13.6 Ma) were also recorded in the Dingjie area. The Cuonadong Dome also records three periods of magmatic activity, 32.0 Ma, 20.2 Ma, and 14.2 Ma [43]. Zircon age of tourmaline-bearing muscovite granites in the Luozha area is 17.7 Ma [56].

There are also some ages of rare metal mineralization in the Himalaya. Qin et al. (2021) reported the age of 25–24 Ma from spodumene pegmatite in the Qiongjiagang area, and which is further interpreted as the metallogenic age of lithium deposit [57]. Spodumene pegmatites of 25–23 Ma are also reported in the Pusila pluton in the Higher Himalaya [58]. The ore-forming rocks closely related to Be–W–Sn rare metal mineralization in Cuonadong Dome are highly differentiated muscovite granites, whose formation age is 16–14 Ma [15,59].

In the Lalong Dome, leucogranites including two-mica granites, albite granites, and pegmatites yielded monazite $^{208}Pb/^{232}Th$ ages of 23.6 ± 0.1 Ma, 21.9 ± 0.1 Ma, and 20.6 ± 0.1 Ma, respectively, which are interpreted as the timing of crystallization of these leucogranites in the Lalong Dome. At the same time, the timing of crystallization gradually becomes new from two-mica granites to albite granites and pegmatites, and the crystallization differentiation of the magma lasted for 3 Ma (from 23.6 Ma to 20.6 Ma). Albite granite yielded a columbite Pb/U age of 20.9 ± 0.5 Ma, which is interpreted as the timing of Be–Nb–Ta rare metal mineralization in the Lalong deposit. These data are interpreted to indicate that the time of albite granite crystallization occurred at 21.9 Ma with the U–Pb monazite age, and the timing of albite granite-type Be–Nb–Ta rare metal mineralization occurred at 20.9 Ma with U–Pb columbite age.

7.2. Petrogenesis of Highly Differentiated Leucogranites in the Lalong Dome

Many classical models have been proposed for the genesis of Himalaya leucogranites, and the representative models are as follows: (1) water-rich melting [60,61]; (2) dehydration and melting under reduced pressure [62]; (3) melting caused by friction heat generation such as STDS and MCT [63]; (4) superheated melting caused by the accumulation of large amounts of radioactive materials [64]; (5) from superheated melting of the thickened crust [65]; (6) highly crystalline differentiation [9]. Among them, partial melting of the HHS and intense crystal fractionation for leucogranites comprise the typical and controversial views in the literature. Previous researchers have suggested that the Himalayan leucogranites, generally belong to the S-type granite, are derived from the metapelites of the Tethys Himalayan Sedimentary Sequence (THS), and are characterized by high silica content (>70 wt.%), peraluminous compositions (A/CNK > 1.1), low content of TiO_2, FeO^T and MgO, high initial $^{87}Sr/^{86}Sr$ ratios ranging from 0.73 to 0.78, and low εNd(t) values ranging from −10 to −15 [8,10,14].

Compared to the typical Himalayan leucogranites, leucogranites in the Lalong Dome, including two-mica granites, muscovite granites, albite granites, and pegmatites, are characterized by high SiO_2 content (>73 wt.%), peraluminous with high Al_2O_3 content (13.6–15.2 wt.%) and A/CNK (mostly > 1.1), low content of TiO_2, CaO, and MgO. At the same time, these leucogranites exhibit the enrichment of Rb, Th, U, and the depletion of Ba, Nb, Zr, Sr, and Ti, strong negative Eu anomalies, and low εNd(t) values ranging from −12.7 to −9.77. These features indicate that the Lalong leucogranites were originally derived from a metasedimentary protolith, showing the features of crust-derived high potassium calc-alkaline and peraluminous S-type granite. In the discrimination diagrams (Figure 13A,B), the Lalong leucogranites are generally plotted in the field of S-type granite.

Moreover, in the Rb/Ba versus Rb/Sr discrimination diagram, most leucogranites are plotted in the fields of clay-rich sources and nearly calculated pelite-derived melt (Figure 13C), these clay-rich sedimentary rocks are probably the major source rocks of S-type granitic magma in the Lalong Dome. The source rocks of these leucogranites should be derived from HHC metasedimentary rocks. Similar source rocks of leucogranites were also reported in other domes in the NHGDs. In the Rb/Sr versus Ba discrimination diagram, leucogranites in the Lalong Dome were derived from muscovite dehydration melting under the water-absent condition (Figure 13D), which possibly resulted from the structural decompression responding to the activity of the STDS [9].

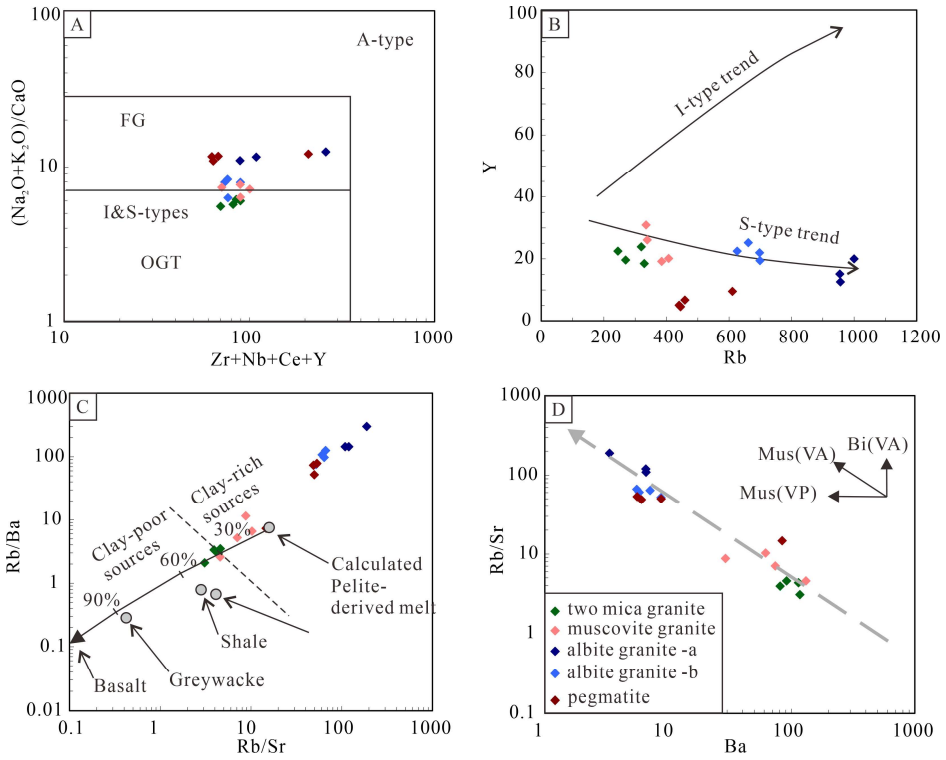

Figure 13. (**A**) Zr + Nb + Ce + Y versus $(Na_2O + K_2O)/CaO$ showing A-type granites and fields for fractionated felsic granites (FG) and unfractionated M-, I- and S-type granites (OGT); the coordinates of these fields are X = 350, Y = 4 and 16 (A) [66]. (**B**) Y vs. Rb diagram [67]. (**C**) Rb/Sr vs. Rb/Ba plots of the granitic rocks [68]. (**D**) Ba–Rb/Sr diagram. Mus (VP)—muscovite melting alteration in saturated vapor phase; Mus (VA)—muscovite melting alteration without vapor phase; Bi (VA)—biotite melting alteration without vapor phase.

Based on the field observation using petrography, there is geochronological, and geochemical evidence that indicates that two-mica granites, muscovite granites, albite granites, and pegmatites in the Lalong Dome are cogenetic leucogranites with the close spatial and temporal relationships. The crystallization age of albite granites is 21.9 Ma, which is younger the crystallization age of 23.6 Ma two-mica granites. Albite granites have lower content of TiO_2, CaO and MgO, Ba, Sr, $^{87}Sr/^{86}Sr(i)$ ratio, $\varepsilon Nd(t)$ values, and higher content of Rb than that of the two-mica granites; these imply a continuous magma fractional crystallization process from two-mica granites through muscovite granites to albite granites and pegmatites.

Wu et al. (2017) reported the typical characteristics of highly fractionated granite, including geology, petrology, mineralogy, rare metal metallogeny, and geochemistry. In terms of geology and petrology, both aplite and pegmatite are important petrological indicators to identify magmatic differentiation; meanwhile, albite granite is generally thought as the product of extreme fractionation of a granitic magma. In the Lalong Dome, albite granite and pegmatite are widely exposed in the core and middle unit of the dome.

In terms of mineralogy, elbaite, lepidolite, or lithium-bearing muscovite is the most important mineralogical mark for highly fractionated granite. At the same time, beryl and columbite–tantalite are typical minerals in highly fractionated granite. In the Lalong Dome, although elbaite and lepidolite have not yet been discovered, lithium-bearing muscovite and columbite–tantalite widely occur in the albite granite and pegmatite. Beryl is always widely hosted in pegmatite. In terms of rare metal metallogeny, the most fractionated granite is often called rare metal granite, since it is closely associated with mineralization of Li, Be, Nb, Ta, Rb, Cs, W, Sn, and REEs. In the Lalong Dome, Be–Nb–Ta rare metal ore bodies are mainly hosted by albite granite and pegmatite. In terms of geochemistry, most highly fractionated granites are characterized by strong peraluminous. During magmatic differentiation, concentrations of Cr, Ni, Co, Sr, Ba, and Zr, decrease, while Li, Rb, and Cs increase. Meanwhile, Zr/Hf = 26 could be used to distinguish magma and hydrothermal granitic systems [69]. Highly fractionated granites are characterized by the decreasing concentrations of REEs, more negative Eu anomalies, and REE tetrad effects [70]. In the Lalong Dome, two-mica granite, muscovite granites, albite granites, and pegmatites are peraluminous. Albite granites have lower content of Ba, Sr, $^{87}Sr/^{86}Sr(i)$ ratio, $\varepsilon Nd(t)$ values, and higher content of Rb (Figure 14A,B) and REEs than that of two-mica granites. All Zr/Hf ratios of these leucogranites are less than 26. Except for two-mica granites ($TE_{1,3} < 1.1$), the $TE_{1,3}$ values in muscovite granites, albite granites, and pegmatites are more than 1.10.

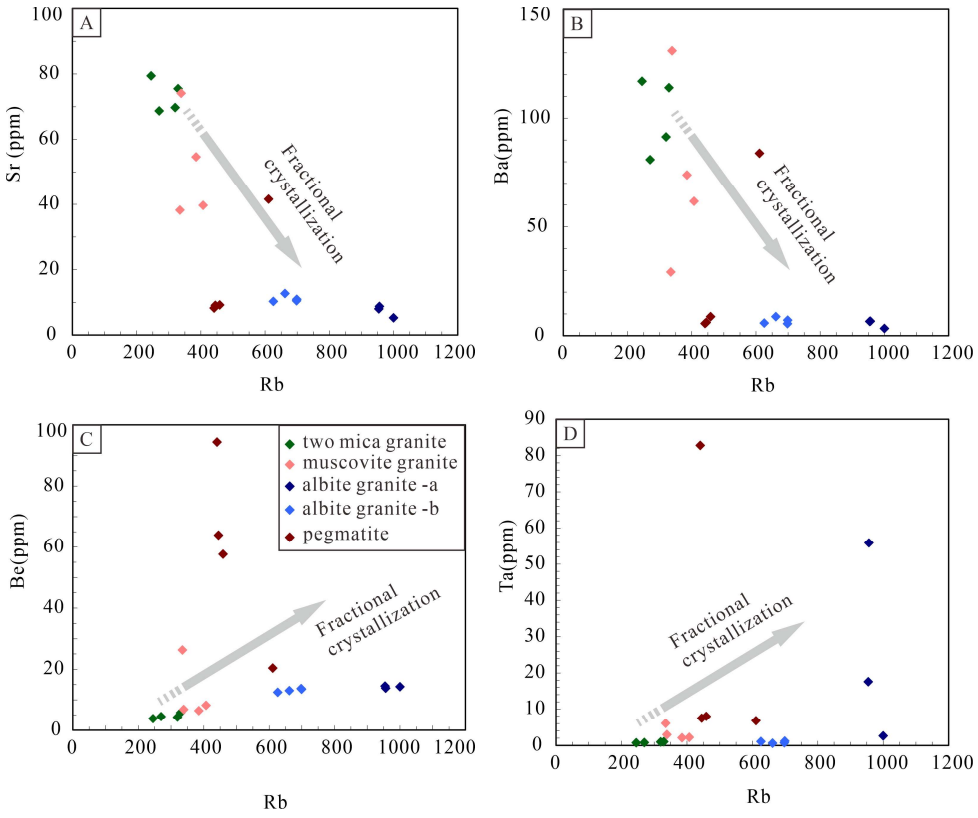

Figure 14. Harker variation diagrams for trace elements, showing fractional crystallization trend. (**A**) Rb vs. Sr diagram. (**B**) Rb vs. Ba diagram. (**C**) Rb vs. Be diagram. (**D**) Rb vs. Ta diagram.

In short, two-mica granites, muscovite granites, albite granites, and pegmatites in the Lalong Dome are all highly differentiated granites, among which albite granites and pegmatites are more differentiated (Figure 14A–D).

7.3. The Relationship between Highly Fractionated Leucogranites and Nb–Ta–Be Rare Metal Mineralization in the Lalong Dome

Rare metal granites are often highly evolved granites, characterized by a specific geochemical signature, such as elevated concentrations in fluxing elements (Li, F, B, P), sig-

nificant depletions in REE, Y, Ca, Fe, Ba, and Sr and marked enrichments in rare lithophile elements and metals (Be, Nb, Ta, Sn, Cs, Rb, and W) [6,8,18,71–75]. These features make them important sources of a wide range of commodities, including strategic metals, industrial minerals, and gemstones. Rare metal granites with specific geochemical signatures are the result of combined magmatic and hydrothermal processes. Three main stages are recognized in the genesis of most rare metal granites: (1) the magmatic stage, which is characterized by crystal fractionation and accessory/minor mineral saturation; (2) the magmatic–hydrothermal transition stage is characterized by fluid-melt element partitioning; and (3) the hydrothermal process, corresponding to the segregation and collection of magmatic fluids in the intragranitic vein system, and followed by metasomatic transformations and a late sulphide stage [6,71,76–79]. Ballouard et al. (2016) proposed that the Nb/Ta ratio of ~5 in the peraluminum granite can serve as a transition value between normal magmatic differentiation and magmatic–hydrothermal interactions. When whole-rock Nb/Ta value is below ~5, the rare metal granites system begins to enter the magmatic–hydrothermal transition stage, which commonly shows evidence of important metasomatism such as albitization and greisenization.

In the Lalong Dome, the geochemical results show that the differentiation index (Di) gradually strengthens from two-mica granite, muscovite granite, and albite granite–pegmatite, in which albite granite to pegmatite are highest, the Di value can reach 94 (Figure 15A–C). The differentiation index Di = Q (quartz) + Or (orthoclase) + Ab (albite) + Ne (nepheline) + Lc (leucite) + Kp (kalsilite), and those content was calculated by CIPW. REE tetrad effects gradually strengthened (Figure 15A), in addition to two-mica granite, the $TE_{1,3}$ values of muscovite granite, albite granite, and pegmatite albite granite are all greater than 1. In addition, the Eu* value and $(La/Yb)_N$ ratio decreased gradually from two-mica granite, muscovite granite, and albite granite–pegmatite, indicating that the crystallization differentiation increased successively (Figure 15D). The high differentiation and hydrothermal evolution of granitic magmas are usually the key mechanisms for the gradual enrichment and mineralization of rare metal elements and volatiles [80,81]. With the ongoing of granitic magma fractional crystallization, a composition of residual magma that is close to eutectic forms; this magma is characterized by the enrichment in Na, K, Al, and Li, Rb, Cs, Be, Nb, Ta, volatile H_2O, P, and B. Roda-Robles et al. (2018) reported petrogenetic relationships between Variscan granitoids and Li–(F–P)-rich aplite–pegmatites in the Central Iberian Zone. Two-mica peraluminous leucogranites and P-rich highly peraluminous granites are interpreted to derive mainly from the partial melting of highly peraluminous, Ca-poor and P-rich Neoproterozoic metasediments. The melts are presumed to evolve through being favored by a high content in fluxing components, such as Li, F, B, P, and H_2O, which contributed to the lowering of viscosity, solidus temperature, and polymerization degree, which is in parallel to the increasing of the diffusion rates and mobility of the highly fractionated melts. Idoia Garate-Olave et al. (2020) discussed the whole-rock composition of the distinguished lithotypes in the Tres Arroyos Granitic Aplite–pegmatite Field (Central Iberian Zone, Spain); they asserted that it reflects similar tendencies to mineral chemistry, supporting a single path of fractional crystallization from the parental Nisa–Alburquerque monzogranite up to the most evolved Li-rich aplite–pegmatites. Therefore, leucogranites in the Lalong Dome belong to rare metal granite.

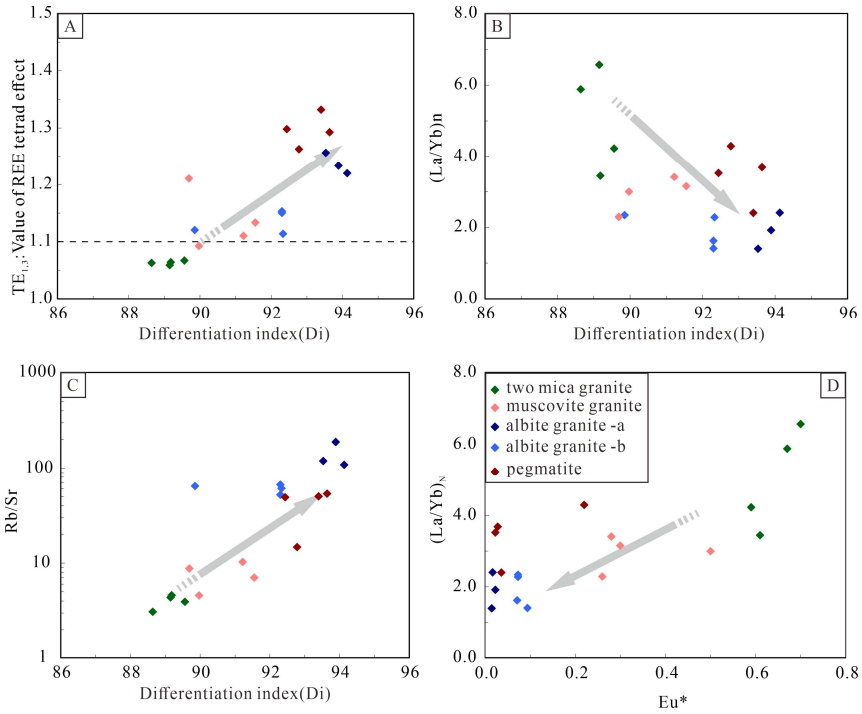

Figure 15. (**A**) The differentiation index (Di) vs. $TE_{1,3}$ diagram. (**B**) The differentiation index (Di) vs. $(La/Yb)_N$ diagram. (**C**) The differentiation index (Di) vs. Rb/Sr diagram. (**D**) Eu* vs. $(La/Yb)_N$ diagram.

Both the Nb/Ta and K/Rb ratios can be used to identify the metallogenic potential of rare metal granites [6,79]. Nb/Ta < 5 and K/Rb < 150 indicate good metallogenic potential of rare metal granites. The ratios of Nb/Ta and Zr/Hf decreased gradually from two-mica granite, muscovite granite, and albite granite–pegmatite, and the ratios of albite granite and pegmatite were less than 5 and 18, respectively. They fall in the area of rare metal granite (Ta–Cs–Li–Nb–Be–Sn–W) (Figure 16A). In the Nb/Ta–K/Rb diagram, the Nb/Ta and K/Rb ratios of albite granite and pegmatite are less than 5 and 150, respectively, indicating that albite granite and pegmatite belong to rare metal granites and have excellent potential for rare metal mineralization (Figure 16B). In addition, from two-mica granite, muscovite granite, and albite granite–pegmatite, Sn and Cs content in these leucogranites gradually increase with the decrease in the Nb/Ta ratio, also showing that the mineralization potential of rare metal increases gradually with the increase in crystallization differentiation, and the potential of albitite granite and pegmatite is the highest (Figure 16C,D).

The Lalong albite granite-type Be–Nb–Ta rare metal ore bodies are hosted by albite granite and pegmatite, which are also plotted in the magmatic–hydrothermal domain, suggesting that albite granite and pegmatite not only experienced the magmatic process, but also experienced the magmatic–hydrothermal transition process as well as a later hydrothermal process. Be–Nb–Ta rare metal in the magmatic stage generates the pre-concentrations and preliminary enrichment and can be hydrothermally redistributed to form large economic deposits during the magmatic–hydrothermal stage (Figure 17).

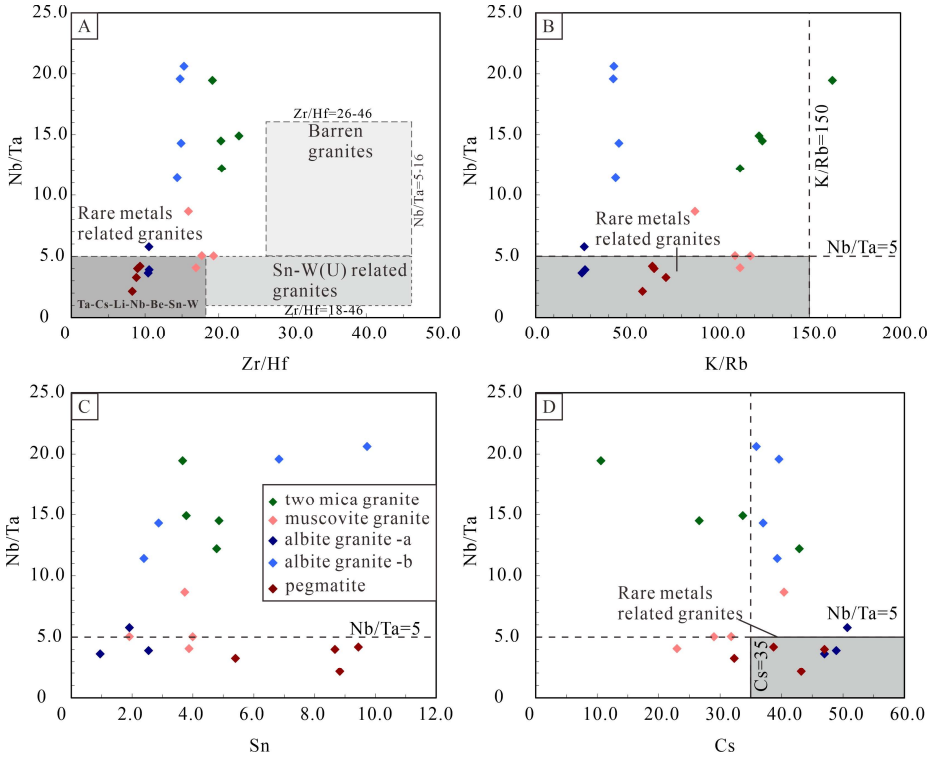

Figure 16. Discrimination diagram of rare metal mineralization potential of leucogranites in the Lalong Dome. (**A**) Zr/Hf vs. Nb/Ta diagram. (**B**) K/Rb vs. Nb/Ta diagram. (**C**) Sn vs. Nb/Ta diagram. (**D**) Cs vs. Nb/Ta diagram.

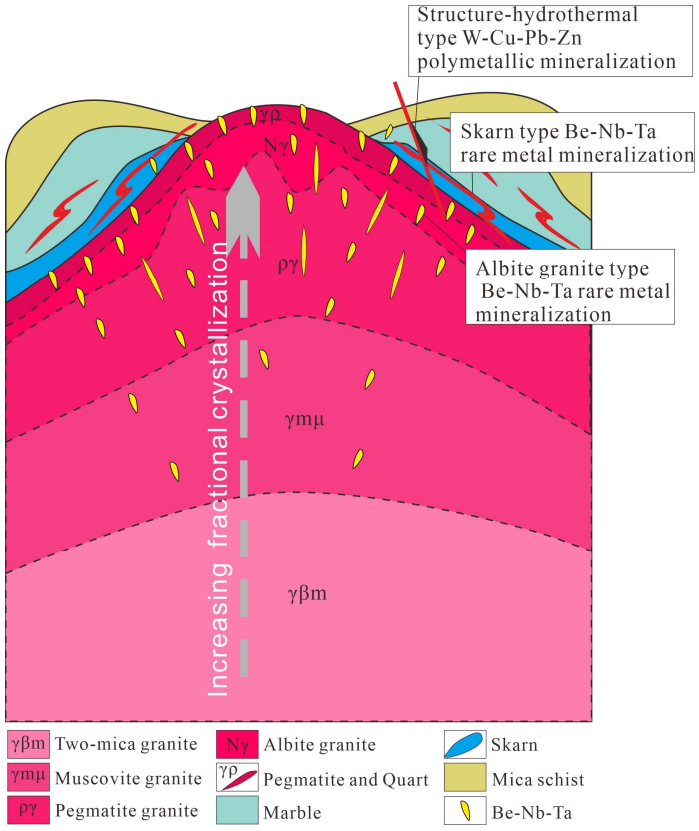

Figure 17. Sketch model for the relationship between magma fractional crystallization in leucogranites and Nb–Ta–Be rare metal mineralization in the Lalong Dome.

7.4. Economic Potential of Rare Metal Leucogranites in the Tethyan Himalaya

Two leucogranite zones have been recognized in the Himalayan orogenic belt: the higher Himalayan leucogranite zone and the Tethyan Himalayan leucogranite zone. Both leucogranites in Higher and Tethyan Himalaya are often highly evolved granites and are named as rare metal granites, with Li, Be, Nb, Ta, W, and Sn mineralization. In the higher Himalayan granite, Qin et al. (2021) reported that there are dozens of spodumene pegmatite dikes in the Qiongjiagang area, and prospective Li_2O resources are estimated at 1,012,500 tons, which suggested that the predicted lithium resources have reached a super large scale. Spodumene, elbaite, and lepidolite have been identified in the highly fractionated leucogranites and associated pegmatites in Pusila area near Mount Everest in the higher Himalaya [58].

The Tethyan Himalayan leucogranites are always exposed in the domes in the NHGDs. In the Tethyan Himalayan granites, through exploration and evaluation, Li et al. (2017) first discovered the super-large-scale Cuonadong skarn-type Be–W–Sn rare metal deposit in the Cuonadong Dome in the eastern Himalayan belt. Later, Li and Be mineralization and Nb–Ta–W mineralization have been reported in the Kuju leucogranites [20] and Xiaru leucogranites from the Xiaru Dome [19], respectively. Wang et al. (2017) reported that the Himalayan leucogranites are commonly related to the rare metal mineralization and warrants future investigation. These important findings show that the Tethyan Himalayan leucogranites have great potential for mineralization of rare metal such as Li, Be, Nb, Ta, W, Sn, and Rb. There are three types of rare metal mineralization in the Lalong Dome: skarn-type Be–Nb–Ta rare metal mineralization, albite granite-type Be–Nb–Ta rare metal mineralization, and structure-hydrothermal-type W–Cu–Pb–Zn polymetallic mineralization. The discovery of the Lalong albite granite Be–Nb–Ta rare metal deposit not only enriches the metallogenic types and potential of the rare metal in the Tethyan Himalaya, but also confirm that Himalayan leucogranites have considerable potential for rare metal mineralization.

8. Conclusions

The field observations and geochronological and geochemical data for leucogranites in the Lalong Dome demonstrate the following findings:

(1) Leucogranites in the Lalong Dome are composed of two-mica granite, muscovite granite, albite granite, and pegmatite from core to rim. Albite granite-type Be–Nb–Ta rare metal ore bodies are hosted by albite granite and pegmatite.

(2) In the Lalong Dome, two-mica granites, albite granites, and pegmatites yielded monazite ages of 23.6 Ma, 21.9 Ma, and 20.6 Ma, respectively, which are interpreted as the timing of crystallization of these leucogranites. The timing of crystallization gradually becomes new from two-mica granites to albite granites and pegmatites, and the crystallization differentiation of the magma lasted for 3 Ma (from 23.6 Ma to 20.6 Ma). The timing of albite granite-type Be–Nb–Ta rare metal mineralization occurred at 20.9 Ma with U–Pb columbite age.

(3) The Lalong leucogranites are crust-derived high-potassium calc-alkaline and peraluminous S-type granites; they were derived from muscovite dehydration melting under the water-absent condition, which possibly resulted from the structural decompression responding to the activity of STDS.

(4) Two-mica granites, muscovite granites, albite granites, and pegmatites in the Lalong Dome are all highly differentiated granites, among which albite granites and pegmatites are more differentiated. Geochemical data imply a continuous magma fractional crystallization process from two-mica granites through muscovite granites to albite granites and pegmatite.

(5) Albite granite and pegmatite belong to rare metal granites and have excellent potential for rare metal mineralization. From two-mica granite, muscovite granite, albite granite, to pegmatite, the mineralization potential of rare metal increases gradually with the increase in crystallization differentiation, and the potential of albite granite

and pegmatite is the highest. Albite granite and pegmatite not only experienced magmatic process, but also magmatic–hydrothermal transition process as well as a later hydrothermal process. Be–Nb–Ta rare metal in the magmatic stage generates the pre-concentrations and preliminary enrichment and can be hydrothermally redistributed to form large economic deposits during the magmatic–hydrothermal stage.

(6) Combined with the discoveries of other deposits in the Himalaya and the occurrence of Be-, Nb/Ta-, and Li-bearing rare metal minerals in leucogranites, the discovery of the Lalong albite granite Be–Nb–Ta rare metal deposit confirms that Himalayan leucogranites have considerable potential for rare metal mineralization.

Supplementary Materials: The following supporting information can be downloaded at https://www.mdpi.com/article/10.3390/min13111456/s1. Table S1: Monazite U–Th–Pb isotopic data were obtained by LA-ICPMS for leucogranities from Lalong Dome; Table S2: U–Pb isotopic data for columbite of Lalong albite granite obtained by LA–ICPMS; Table S3: Major- and trace-element compositions of leucogranities from Lalong Dome; Table S4: Sr–Nd isotopic compositions of leucogranites from Lalong Dome.

Author Contributions: Writing—original draft preparation, J.F.; writing—review and editing, G.L. and G.W.; methodology, W.G. and W.L.; investigation, S.D. and W.L.; data curation, Y.J. and H.Z.; formal analysis, Y.L. All authors have read and agreed to the published version of the manuscript.

Funding: This research was funded by the National Natural Science Foundation of China (grant no. 91955208), the Second Tibetan Plateau Scientific Expedition and Research Program (STEP, grant no. 2019QZKK0806), Ministry of Science and Technology Program (2021YFC2901903, 2023YFC2908400), and China Geological Survey Program (DD20230337 and DD20230281).

Data Availability Statement: The data presented in this study are openly available online at Supplementary Materials.

Acknowledgments: Guotao Ma, Shengxian Liang, Hongzhao Shi, Chen Ling, and Yuling Yang are thanked for their assistance in the field investigations. We are also grateful to Huan Hu at the State Key Laboratory of Metallogenic Mechanism of Endogenous Metal Deposits, Nanjing University, China for assistance with the monazite U–Th–Pb and columbite U–Pb dating analysis. Limin Zhou is thanked for Sr and Nd isotope analysis.

Conflicts of Interest: The authors declare no conflict of interest.

References

1. Roda-Robles, E.; Vieira, R.; Lima, A.; Errandonea-Martin, J.; Pesquera, A.; Cardoso-Fernandes, J.; Garate-Olave, I. Li-rich pegmatites and related peraluminous granites of the Fregeneda-Almendra field (Spain-Portugal): A case study of magmatic signature for Li enrichment. *Lithos* **2023**, *452–453*, 107195. [CrossRef]
2. Monnier, L.; Lach, P.; Salvi, S.; Melleton, J.; Bailly, L.; Béziat, D.; Monnier, Y.; Gouy, S. Quartz trace-element composition by LA-ICP-MS as proxy for granite differentiation, hydrothermal episodes, and related mineralization: The Beauvoir Granite (Echassières district), France. *Lithos* **2018**, *320–321*, 355–377. [CrossRef]
3. Garate-Olave, I.; Müller, A.; Roda-Robles, E.; Gil-Crespo, P.; Pesquera, A. Extreme fractionation in a granite–pegmatite system documented by quartz chemistry: The case study of Tres Arroyos (Central Iberian Zone, Spain). *Lithos* **2017**, *286–287*, 162–174. [CrossRef]
4. Pesquera, A.; Gil-Crespo, P.P.; Torres-Ruiz, J.; Roda-Robles, E. Insights into petrogenesis of the Jálama pluton (Central Iberian Zone, western Spain). *Int. Geol. Rev.* **2018**, *60*, 157–187. [CrossRef]
5. Ballouard, C.; Boulvais, P.; Poujol, M.; Gapais, D.; Yamato, P.; Tartese, R.; Cuney, M. Tectonic record, magmatic history and hydrothermal alteration in the Hercynian Guérande leucogranite, Armorican Massif, France. *Lithos* **2015**, *220–223*, 1–22. [CrossRef]
6. Kaeter, D.; Barros, R.; Menuge, J.F.; Chew, D.M. The magmatic–hydrothermal transition in rare-element pegmatites from southeast Ireland: LA-ICP-MS chemical mapping of muscovite and columbite–tantalite. *Geochim. Cosmochim. Acta* **2018**, *240*, 98–130. [CrossRef]
7. Cerný, P.; Ercit, T.S. The classification of granitic pegmatites revisited. *Can. Miner.* **2005**, *43*, 2005–2026. [CrossRef]
8. Wu, F.Y.; Liu, X.C.; Liu, Z.C.; Wang, R.C.; Xie, L.; Wang, J.M.; He, S.X. Highly fractionated Himalayan leucogranites and associated rare-metal mineralization. *Lithos* **2020**, *352–353*, 105319. [CrossRef]
9. Wu, F.; Liu, Z.; Liu, X.; Ji, W. Himalayan leucogranite: Petrogenesis and implications to orogenesis and plateau uplift. *Acta Petrol. Sin.* **2015**, *31*, 1–36, (In Chinese with English Abstract).

10. Wu, F.; Liu, X.; Ji, W.; Wang, J.; Yang, L. Highly fractionated granites: Recognition and research. *Sci. China Earth Sci.* **2017**, *60*, 1201–1219. [CrossRef]
11. Liu, Z.-C.; Wu, F.-Y.; Liu, X.-C.; Wang, J.-G.; Yin, R.; Qiu, Z.-L.; Ji, W.-Q.; Yang, L. Mineralogical evidence for fractionation processes in the Himalayan leucogranites of the Ramba Dome, southern Tibet. *Lithos* **2019**, *340–341*, 71–86. [CrossRef]
12. Wang, Z.Z.; Liu, S.A.; Liu, Z.C.; Zheng, Y.C.; Wu, F.Y. Extreme Mg and Zn isotope fractionation recorded in the Himalayan leucogranites. *Geochim. Cosmochim. Acta* **2020**, *278*, 305–321. [CrossRef]
13. Liu, Z.C.; Wu, F.Y.; Ji, W.Q.; Wang, J.G.; Liu, C.Z. Petrogenesis of the Ramba leucogranite in the Tethyan Himalaya and constraints on the channel flow model. *Lithos* **2014**, *208–209*, 118–136. [CrossRef]
14. Liu, Z.C.; Wu, F.Y.; Ding, L.; Liu, X.C.; Wang, J.G.; Ji, W.Q. Highly fractionated Late Eocene (~35 Ma) leucogranite in the Xiaru Dome, Tethyan Himalaya, South Tibet. *Lithos* **2016**, *240–243*, 337–354. [CrossRef]
15. Li, G.M.; Zhang, L.K.; Jiao, Y.J.; Xia, X.B.; Dong, S.L.; Fu, J.G.; Huang, Y. First discovery and implications of Cuonadong superlarge Be–W–Sn polymetallic deposit in Himalayan metallogenic belt, southern Tibet. *Miner. Depos.* **2017**, *36*, 1003–1008. (In Chinese with English Abstract)
16. Fu, J.; Li, G.; Wang, G.; Zhang, L.; Liang, W.; Zhang, X.; Jiao, Y.; Huang, Y. Structural and thermochronologic constraints on skarn rare-metal mineralization in the Cenozoic Cuonadong Dome, Southern Tibet. *J. Asian Earth Sci.* **2020**, *205*, 104612. [CrossRef]
17. Li, G.M.; Zhang, L.K.; Zhang, Z.; Xia, X.B.; Liang, W.; Hou, C.Q. New exploration progresses, resource potentials and prospecting targets of strategic minerals in the southern Qinghai-Tibet Plateau. *Sediment. Geol. Tethyan Geol.* **2021**, *41*, 351–360. (In Chinese with English Abstract)
18. Wang, R.; Wu, F.; Xie, L.; Liu, X.; Wang, J.; Yang, L.; Lai, W.; Liu, C. A preliminary study of rare-metal mineralization in the Himalayan leucogranite belts, South Tibet. *Sci. China Earth Sci.* **2017**, *60*, 1655–1663. [CrossRef]
19. Xie, L.; Wang, R.C.; Tian, E.N.; Liu, Z.C.; Wu, F.Y.; Liu, X.C.; Liu, C. Oligocene Nb-Ta-W-mineralization related to the Xiaru leucogranite in the Himalayan Orogen. *Chin. Sci. Bull.* **2021**, *66*, 4574–4591, (In Chinese with English Abstract). [CrossRef]
20. Zhou, Q.; Qin, K.; He, C.; Wu, H.; Liu, Y.; Niu, X.; Mo, L.; Liu, X.; Zhao, J. Li–Be–Nb–Ta mineralogy of the Kuqu leucogranite and pegmatite in the Eastern Himalaya, Tibet, and its implication. *Acta Petrol. Sin.* **2021**, *37*, 3305–3324. (In Chinese with English Abstract)
21. Fu, J.G.; Li, G.M.; Dong, S.L.; Zhang, H.; Guo, W.K.; Zhang, L.K.; Ling, C. Mineral chemistry of garnet and its implication for the magmatic-hydrothermal transition in rare metal leucogranites in the Lalong dome, southern Tibet, China. *Sediment. Geol. Tethyan Geol.* **2022**, *42*, 288–299, (In Chinese with English Abstract).
22. Fu, J.; Li, G.; Wang, G.; Dong, S.; Zhang, H.; Guo, W.; Zhang, L.; Zhang, X.; Jiao, Y. Geological Characteristics and Metallogenic Types of Be-Nb-Ta Rare Metals in the Lalong Dome, Southern Tibet, China. *Geotecton. Metallog.* **2021**, *45*, 913–933. (In Chinese with English Abstract)
23. Fu, J.G.; Li, G.M.; Dong, S.L.; Zhang, H.; Guo, W.K.; Zhang, L.K.; Jiao, Y.J. Identification and its significances of the Lalong Be-Nb-Ta-bearing albite granite in the Northern Himalaya, Tibet. *Sediment. Geol. Tethyan Geol.* **2020**, *40*, 91–103. (In Chinese with English Abstract)
24. Wang, E.; Burchfiel, B.C. Interpretation of Cenozoic Tectonics in the Right-Lateral Accommodation Zone between the Ailao Shan Shear Zone and the Eastern Himalayan Syntaxis. *Int. Geol. Rev.* **1997**, *39*, 191–219. [CrossRef]
25. Edwards, M.A.; Pêcher, A.; Kidd, W.S.F.; Burchfiel, B.C.; Royden, L.H. Southern Tibet Detachment System at Khula Kangri, Eastern Himalaya: A Large-Area, Shallow Detachment Stretching into Bhutan? *J. Geol.* **1999**, *107*, 623–631. [CrossRef]
26. Zhang, J.; Santosh, M.; Wang, X.; Guo, L.; Yang, X.; Zhang, B. Tectonics of the northern Himalaya since the India–Asia collision. *Gondwana Res.* **2012**, *21*, 939–960. [CrossRef]
27. Lee, J.; Hacker, B.; Wang, Y. Evolution of North Himalayan gneiss domes: Structural and metamorphic studies in Mabja Dome, southern Tibet. *J. Struct. Geol.* **2004**, *26*, 2297–2316. [CrossRef]
28. Liang, W.; Yang, Z.S.; Zheng, Y.C. The Zhaxikang Pb–Zn deposit: Ar–Ar age of sericite and its metallogenic significance. *Acta Geol. Sin.* **2015**, *89*, 560–568, (In Chinese with English Abstract).
29. Xie, Y.; Li, L.; Wang, B.; Li, G.; Liu, H.; Li, Y.; Dong, S.; Zhou, J. Genesis of the Zhaxikang epithermal Pb-Zn-Sb deposit in southern Tibet, China: Evidence for a magmatic link. *Ore Geol. Rev.* **2017**, *80*, 891–909. [CrossRef]
30. Yang, Z.; Hou, Z.; Meng, X.; Liu, Y.; Fei, H.; Tian, S.; Li, Z.; Gao, W. Post-collisional Sb and Au mineralization related to the South Tibetan detachment system, Himalayan orogen. *Ore Geol. Rev.* **2009**, *36*, 194–212. [CrossRef]
31. Lee, J.; Hacker, B.R.; Dinklage, W.S.; Wang, Y.; Gans, P.; Calvert, A.; McClelland, W. Evolution of the Kangmar Dome, southern Tibet: Structural, petrologic, and thermochronologic constraints. *Tectonics* **2000**, *19*, 872–895. [CrossRef]
32. Lee, J.; Hager, C.; Wallis, S.R.; Stockli, D.F.; Whitehouse, M.J.; Aoya, M.; Wang, Y. Middle to late Miocene extremely rapid exhumation and thermal reequilibration in the Kung Co rift, southern Tibet. *Tectonics* **2011**, *30*, 1–26. [CrossRef]
33. Chen, Z.; Liu, Y.; Hodges, K.V.; Burchfiel, B.C.; Royden, L.H.; Deng, C. The Kangmar Dome: A metamorphic core complex in southern Xizang (Tibet). *Science* **1990**, *250*, 1552–1556. [CrossRef] [PubMed]
34. Langille, J.; Lee, J.; Hacker, B.; Seward, G. Middle crustal ductile deformation patterns in southern Tibet: Insights from vorticity studies in Mabja Dome. *J. Struct. Geol.* **2010**, *32*, 70–85. [CrossRef]
35. Langille, J.M.; Jessup, M.J.; Cottle, J.; Ahmad, T. Kinematic and thermal studies of the Leo Pargil Dome: Implications for synconvergent extension in the NW Indian Himalaya. *Tectonics* **2014**, *33*, 1766–1786. [CrossRef]

36. Fu, J.; Li, G.; Wang, G.; Huang, Y.; Zhang, L.; Dong, S.; Liang, W. First field identification of the Cuonadong dome in southern Tibet: Implications for EW extension of the North Himalayan gneiss dome. *Int. J. Earth Sci.* **2017**, *106*, 1581–1596. [CrossRef]
37. Jessup, M.J.; Langille, J.M.; Cottle, J.M.; Ahmad, T. Crustal thickening, Barrovian metamorphism, and exhumation of midcrustal rocks during doming and extrusion: Insights from the Himalaya, NW India. *Tectonics* **2016**, *35*, 160–186. [CrossRef]
38. Zhang, J.; Yang, X.; Qi, G.; Wang, D. Geochronology of the Malashan dome and its application in formation of the Southern Tibet detachment system (STDS) and Northern Himalayan gneiss domes (NHGD). *Acta Petrol. Sin.* **2011**, *27*, 3535–3544. (In Chinese with English Abstract)
39. Zhang, J.; Guo, L.; Zhang, B. Structure and kinematics of the Yalashanbo dome in the Northern Himalayan dome belt, China. *Chin. J. Geol.* **2007**, *42*, 16–30, (In Chinese with English Abstract).
40. Fu, J.; Li, G.; Wang, G.; Zhang, L.; Liang, W.; Zhang, Z.; Huang, Y. Synchronous granite intrusion and E–W extension in the Cuonadong dome, southern Tibet, China: Evidence from field observations and thermochronologic results. *Int. J. Earth Sci.* **2018**, *107*, 2023–2041. [CrossRef]
41. Quigley, M.; Yu, L.; Liu, X.; Wilson, C.J.; Sandiford, M.; Phillips, D. 40Ar/39Ar thermochronology of the Kampa Dome, southern Tibet: Implications for tectonic evolution of the North Himalayan gneiss domes. *Tectonophysics* **2006**, *421*, 269–297. [CrossRef]
42. Wagner, T.; Lee, J.; Hacker, B.R.; Seward, G. Kinematics and vorticity in Kangmar Dome, southern Tibet: Testing midcrustal channel flow models for the Himalaya. *Tectonics* **2010**, *29*, 1–26. [CrossRef]
43. Fu, J.; Li, G.; Wang, G.; Zhang, L.; Liang, W.; Zhang, X.; Huang, Y. Structural analysis of sheath folds and geochronology in the Cuonadong Dome, southern Tibet, China: New constraints on the timing of the South Tibetan detachment system and its relationship to North Himalayan Gneiss Domes. *Terra Nova* **2020**, *32*, 300–323. [CrossRef]
44. Fu, J.; Li, G.; Wang, G.; Zhang, L.; Liang, W.; Zhang, X.; Jiao, Y.; Dong, S. Structural and kinematic analysis of the Cuonadong dome, southern Tibet, China: Implications for middle-crust deformation. *J. Asian Earth Sci. X* **2022**, *8*, 100112. [CrossRef]
45. Che, X.D.; Wu, F.Y.; Wang, R.C.; Gerdes, A.; Ji, W.Q.; Zhao, Z.H.; Zhu, Z.Y. In situ U–Pb isotopic dating of columbite–tantalite by LA–ICP–MS. *Ore Geol. Rev.* **2015**, *65*, 979–989. [CrossRef]
46. Griffin, W.L.; Powell, W.J.; Pearson, N.J.; O'Reilly, S.Y. *GLITTER: Data Reduction Software for Laser Ablation ICP-MS*; Mineralogical Association of Canada: Québec, QC, Canada, 2008.
47. Ludwig, K.R. *User's Manual for Isoplot/EX Version 3.00: A Geochronological Tool Kit for Microsoft Excel*; Berkeley Geochronology Center, Special Publication: Berkeley, CA, USA, 2003; Volume 4, pp. 1–70.
48. Middlemost, E.A. Naming materials in the magma/igneous rock system. *Earth-Sci. Rev.* **1994**, *37*, 215–224. [CrossRef]
49. Maniar, P.D.; Piccoli, P.M. Tectonic discrimination of granitoids. *Geol. Soc. Am. Bull.* **1989**, *101*, 635–643. [CrossRef]
50. Rickwood, P.C. Boundary lines within petrologic diagrams which use oxides of major and minor elements. *Lithos* **1989**, *22*, 247–263. [CrossRef]
51. Jahn, B.M.; Wu, F.; Capdevila, R.; Martineau, F.; Zhao, Z.; Wang, Y. Highly evolved juvenile granites with tetrad REE patterns: The Woduhe and Baerzhe granites from the Great Xing'an Mountains in NE China. *Lithos* **2001**, *59*, 171–198. [CrossRef]
52. Irber, W. The lanthanide tetrad effect and its correlation with K/Rb, Eu/Eu*, Sr/Eu, Y/Ho, and Zr/Hf of evolving peraluminous granite suites. *Geochim. Cosmochim. Acta* **1999**, *63*, 489–508. [CrossRef]
53. Wu, Z.H.; Ye, P.S.; Wu, Z.H.; Zhao, Z. LA-ICP-MS zircon U-Pb ages of tectonic-thermal events in the Yalaxiangbo dome of Tethys Himalayan belt. *Geol. Bull. China* **2014**, *33*, 595–605, (In Chinese with English Abstract).
54. Liu, W.C.; Wang, Y.; Zhang, X.X.; Li, H.M.; Zhou, Z.G.; Zhao, X.G. The rock types and isotope dating of the Kangmar gneissic dome in southern Tibet. *Earth Sci. Front.* **2004**, *11*, 491–501, (In Chinese with English Abstract).
55. Lee, J.; Martin, J. Whitehouse. Onset of mid-crustal extensional flow in southern Tibet: Evidence from U/Pb zircon ages. *Geology* **2007**, *35*, 45–48. [CrossRef]
56. Huang, C.; Zhao, Z.; Li, G.; Zhu, D.C.; Liu, D.; Shi, Q. Leucogranites in Lhozag, southern Tibet: Implications for the tectonic evolution of the eastern Himalaya. *Lithos* **2017**, *294–295*, 246–262. [CrossRef]
57. Qin, K.; Zhao, J.; He, C.; Shi, R. Discovery of the Qiongjiagang giant lithium pegmatite deposit in Himalaya, Tibet, China. *Acta Petrol. Sin.* **2021**, *37*, 3277–3286, (In Chinese with English Abstract). [CrossRef]
58. Liu, C.; Wang, R.C.; Wu, F.Y.; Xie, L.; Liu, X.C.; Li, X.K.; Li, X.J. Spodumene pegmatites from the Pusila pluton in the higher Himalaya, South Tibet: Lithium mineralization in a highly fractionated leucogranite batholith. *Lithos* **2020**, *358–359*, 105421. [CrossRef]
59. Huang, C.; Li, G.; Zhang, Z.; Liang, W.; Huang, Y.; Zhang, L.; Fu, J. Petrogenesis of the Cuonadong leucogranite in south Tibet: Constraints from bulk-rock geochemistry and zircon U-Pb dating. *Earth Sci. Front.* **2018**, *25*, 182–195, (In Chinese with English Abstract).
60. Le Fort, P.; Cuney, M.; Deniel, C.; France-Lanord, C.; Sheppard, S.M.F.; Upreti, B.N.; Vidal, P. Crustal generation of the Himalayan leucogranites. *Tectonophysics* **1987**, *134*, 39–57. [CrossRef]
61. Gao, L.E.; Zeng, L.; Asimow, P.D. Contrasting geochemical signatures of fluid-absent versus fluid-fluxed melting of muscovite in metasedimentary sources: The Himalayan leucogranites. *Geology* **2017**, *45*, 39–42. [CrossRef]
62. Harris, N.; Ayres, M.; Massey, J. Geochemistry of granitic melts produced during the incongruent melting of muscovite: Implications for the extraction of Himalayan leucogranite magmas. *J. Geophys. Res. Solid Earth* **1995**, *100*, 15767–15777. [CrossRef]
63. Mark Harrison, T.; Lovera, O.M.; Grove, M. New insights into the origin of two contrasting Himalayan granite belts. *Geology* **1997**, *25*, 899–902. [CrossRef]

64. Searle, M.P.; Cottle, J.M.; Streule, M.J.; Waters, D.J. Crustal melt granites and migmatites along the Himalaya: Melt source, segregation, transport and granite emplacement mechanisms. *Geol. Soc. Am. Spec. Pap.* **2010**, *472*, 219–233.
65. Thompson, A.B.; Connolly, J.A. Connolly. Melting of the continental crust: Some thermal and petrological constraints on anatexis in continental collision zones and other tectonic settings. *J. Geophys. Res.* **1995**, *100*, 15565–15579. [CrossRef]
66. Whalen, J.B.; Currie, K.L.; Chappell, B.W. A-type granites: Geochemical characteristics, discrimination and petrogenesis. *Contrib. Mineral. Petrol.* **1987**, *95*, 407–419. [CrossRef]
67. Chappell, B.W. Aluminium saturation in I- and S-type granites and the characterization of fractionated haplogranites. *Lithos* **1999**, *46*, 535–551. [CrossRef]
68. Sylvester, P.J. Post-collisional strongly peraluminous granites. *Lithos* **1998**, *45*, 29–44. [CrossRef]
69. Bau, M. Controls on the fractionation of isovalent trace elements in magmatic and aqueous systems: Evidence from Y/Ho, Zr/Hf, and lanthanide tetrad effect. *Contrib. Miner. Pet.* **1996**, *123*, 323–333. [CrossRef]
70. Roda-Robles, E.; Gil-Crespo, P.P.; Pesquera, A.; Lima, A.; Garate-Olave, I.; Merino-Martínez, E.; Errandonea-Martin, J. Compositional Variations in Apatite and Petrogenetic Significance: Examples from Peraluminous Granites and Related Pegmatites and Hydrothermal Veins from the Central Iberian Zone (Spain and Portugal). *Minerals* **2022**, *12*, 1401. [CrossRef]
71. Ballouard, C.; Elburg, M.A.; Tappe, S.; Reinke, C.; Ueckermann, H.; Doggart, S. Magmatic-hydrothermal evolution of rare metal pegmatites from the Mesoproterozoic Orange River pegmatite belt (Namaqualand, South Africa). *Ore Geol. Rev.* **2019**, *116*, 103252. [CrossRef]
72. Fuchsloch, W.C.; Nex, P.A.; Kinnaird, J.A. The geochemical evolution of Nb-Ta-Sn oxides from pegmatites of the Cape Cross–Uis pegmatite belt, Namibia. *Mineral. Mag.* **2019**, *83*, 161–179. [CrossRef]
73. Kontak, D.J. Nature and Origin of an LCT-Suite Pegmatite with Late-Stage Sodium Enrichment, Brazil Lake, Yarmouth County, Nova Scotia. I. Geological Setting and Petrology. *Can. Miner.* **2006**, *44*, 563–598. [CrossRef]
74. David, L. Ore-forming processes within granitic pegmatites. *Ore Geol. Rev.* **2018**, *101*, 349–383.
75. Melcher, F.; Graupner, T.; Gäbler, H.E.; Sitnikova, M.; Oberthür, T.; Gerdes, A.; Chudy, T. Mineralogical and chemical evolution of tantalum–(niobium–tin) mineralisation in pegmatites and granites. Part 2: Worldwide examples (excluding Africa) and an overview of global metallogenetic patterns. *Ore Geol. Rev.* **2017**, *89*, 946–987. [CrossRef]
76. Küster, D.; Romer, R.L.; Tolessa, D.; Zerihun, D.; Bheemalingeswara, K.; Melcher, F.; Oberthür, T. The Kenticha rare-element pegmatite, Ethiopia: Internal differentiation, U–Pb age and Ta mineralization. *Miner. Deposita* **2009**, *44*, 723–750. [CrossRef]
77. Peterková, T.; Dolejš, D. Magmatic-hydrothermal transition of Mo-W-mineralized granite-pegmatite-greisen system recorded by trace elements in quartz: Krupka district, Eastern Krušné hory/Erzgebirge. *Chem. Geol.* **2019**, *523*, 179–202. [CrossRef]
78. Michaud, J.A.S.; Pichavant, M. Magmatic fractionation and the magmatic-hydrothermal transition in rare metal granites: Evidence from Argemela (Central Portugal). *Geochim. Cosmochim. Acta* **2020**, *289*, 130–157. [CrossRef]
79. Ballouard, C.; Poujol, M.; Boulvais, P.; Branquet, Y.; Tartèse, R.; Vigneresse, J.L. Nb-Ta fractionation in peraluminous granites: A marker of the magmatic-hydrothermal transition. *Geology* **2016**, *44*, 231–234. [CrossRef]
80. Garate-Olave, I.; Roda-Robles, E.; Gil-Crespo, P.P.; Pesquera, A.; Errandonea-Martin, J. The Tres Arroyos Granitic Aplite-Pegmatite Field (Central Iberian Zone, Spain): Petrogenetic Constraints from Evolution of Nb-Ta-Sn Oxides, Whole-Rock Geochemistry and U-Pb Geochronology. *Minerals* **2020**, *10*, 1008. [CrossRef]
81. Roda-Robles, E.; Villaseca, C.; Pesquera, A.; Gil-Crespo, P.P.; Vieira, R.; Lima, A.; Garate-Olave, I. Petrogenetic relationships between Variscan granitoids and Li-(F-P)-rich aplite-pegmatites in the Central Iberian Zone: Geological and geochemical constraints and implications for other regions from the European Variscides. *Ore Geol. Rev.* **2018**, *95*, 408–430. [CrossRef]